Spatiotemporal variability of earthquake source parameters at Parkfield, California, and their relationship with the 2004 M6 earthquake

Jiewen Zhang[1], Xiaowei Chen[1], Rachel E. Abercrombie[2]

[1]University of Oklahoma, Norman Oklahoma

[2]Boston University, Boston Massachusetts

Corresponding Author: Jiewen Zhang (jwzhang914@ou.edu)

Key Points:

- Borehole data and an improved spectral decomposition approach provide better constraints on estimates of corner frequency and stress drop.
- Frequency bandwidth, and corrections for variable attenuation and rupture velocity influence stress drop estimates and interpretations.
- Spatial pattern of stress drop is heterogeneous and stable with time, temporal changes of stress drop vary within different fault patches.

Abstract

Earthquake stress drop is an important source parameter that directly links to strong ground motion and fundamental questions in earthquake physics. Stress drop estimations may contain significant uncertainties due to factors such as variations in material properties and data limitations, which limits the applications of stress drop interpretations. Using a high-resolution borehole network, we analyze 4537 earthquakes in the Parkfield area in Northern California between 2001 and 2016 with spectral decomposition and an improved stacking method. To evaluate the influence of spatiotemporal variations of material properties on stress drop estimations, we apply six different strategies to account for spatial variations of velocity and attenuation changes, and divide earthquakes into three separate time periods to correct temporal variations of attenuation. These results show that appropriate corrections can significantly reduce the scatter in stress drop estimations, and decrease apparent depth and magnitude dependence. We further investigate the influence of data limitations on stress drop estimations, and show that insufficient bandwidth may cause systematic underestimation and increased stress drop scatter. The stress drop measurements from the high-frequency borehole recordings exhibit complex stable spatial patterns with no clear correlation with the nature of fault slip, or the slip distribution of the 2004 M6 earthquake. In some regions with the largest numbers of earthquakes, we can resolve temporal variations that indicate stress drop decrease following the 2004 earthquake, and gradual recovery. These temporal variations do not affect the long-term stress drop spatial variations, suggesting local material properties may control the spatial heterogeneity of stress drop.

Plain Language Summary

Earthquake stress drop (the change in shear stress before and after the earthquake) reflects the properties of the fault where earthquakes occur. Determining

the scaling relationships between earthquake stress drop and magnitude enables us to predict the behavior of infrequent large earthquakes from the measurements of the more abundant small earthquakes. Measurement of stress drop is challenging, especially for small earthquakes. Different studies can obtain different stress drop values for the same earthquakes, leading to different interpretations. We use recordings from a high-resolution borehole network in Parkfield, California to measure source parameters for small earthquakes. We examine the influence of data limitation (e.g., frequency bandwidth) and corrections for material properties on stress drop resolution. We find that if the bandwidth is too narrow, the resulting source parameters can be systematically underestimated with large scatter. Insufficient corrections of material properties can lead to biased interpretation of stress drop patterns and scaling relationships. Our final results show that the stress drops of earthquakes in Parkfield do not depend on magnitude or depth, but exhibit strong spatial variations that are stable with time. The 2004 M6 earthquake caused temporal variations of stress drop, and the temporal changes are different at different fault patches.

Keywords

Source parameter, spectral decomposition and stacking method, frequency band, self-similarity, spatiotemporal variability, Parkfield microearthquakes

1 Introduction

The stress drop is a measure of the average stress changes during an earthquake. It is one of the most important source parameters that is directly related to strong ground motion and fundamental problems earthquake physics. It is superficially easy to compute stress drop from spectral analysis based on corner frequency, but the high variability, both within individual studies (e.g., Abercrombie et al., 2017) and between different studies (e.g., Pennington et al., 2021), indicates that stress drop measurements are often subject to large uncertainties (e.g., Abercrombie 2021). Published measurements span 3 orders of magnitude, and until real variability can be distinguished from the large uncertainties, the potential for using stress drop measurements to probe the physics of the rupture process, and to assist in the prediction of future ground motions is severely limited (e.g., Hardebeck, 2020; Molkenthin et al., 2017).

Earthquake stress drop can help understand whether earthquakes with different magnitudes are associated with the same physical processes (self-similarity) (Aki, 1967). Stress drop has been found to be independent of magnitude by multiple studies, and compilations of studies, covering different magnitude ranges, from small and moderate (Allmann & Shearer, 2007; Goebel et al., 2015; Imanishi & Ellsworth, 2006; Uchide et al., 2014) to large ones (Allmann & Shearer, 2009). In contrast, other studies have reported non-self-similarity, typically over smaller magnitude ranges (Imanishi & Uchide, 2017; Mayeda et al., 2005; Oye et al., 2005). Spatial and temporal variations of stress drop have the potential to reveal heterogeneities and changes in stress distribution within fault zones (e.g., Allmann & Shearer, 2007; Chaves et al., 2020; Chen & Shearer, 2013; Moyer et

al., 2018; Ruhl et al., 2017; Shearer et al., 2006a; Uchide et al., 2014)). However, different studies of the same region have resolved different spatial and temporal distributions; for example, the spatial pattern in Japan from (Oth, 2013) appears different from that by Uchide et al., (2014) and Yoshida et al., (2017), who used more localized attenuation corrections. Some studies have also observed an increase in stress drop with depth that may reflect increasing stress on the faults, but such dependence may be, at least partially, an artifact of changes in attenuation and velocity with depth (Allmann & Shearer, 2007; Sumy et al., 2017; Abercrombie et al., 2020). Abercrombie (2014) analyzed three repeating clusters of small earthquakes on the San Andreas Fault at Parkfield, and found the temporal changes of only one cluster (largest magnitudes) agreed with the results of Allmann & Shearer (2007) for the same earthquakes.

The variation in stress drop observed between different earthquakes could be due to real variation in the rupture processes, but the discrepancy among different studies indicates that random and systematic uncertainties are significantly distorting results; the differences between studies are often significantly larger than the calculated uncertainties (e.g., Huang et al., 2017; Pennington et al., 2021). The most likely causes of these problems are the simplifying assumptions required (concerning source geometry and attenuation structure), and the inherent ambiguities in separating source and path effects using seismograms with limited frequency range (e.g., Abercrombie, 2021). Shearer et al. (2019) and Pennington et al. (2021) both demonstrated that relative variability is more reliable than absolute values, and that consistency between different approaches provides confidence in the results.

To understand better the real uncertainties in stress drop estimates, and improve the quality of the measurements, it is important to perform detailed analyses of the effects caused by frequency bandwidth limits of the data, spatiotemporal variations of attenuation, and possible rupture velocity changes, among other things. As the problems became clearer, many studies have focused on reducing the scatter and improving the resolution of stress drop measurements, and quantifying more realistic uncertainty measurements using high-quality datasets and careful data processing. Baltay et al. (2011) showed that results using stacked Empirical Green's Functions (EGF) to correct for path and site effects had much lower standard deviation than previous studies; Kwiatek et al., (2014) found the stress drop scattering from EGF analysis is significantly reduced from fixed attenuation correction. Chen & Abercrombie (2020) used synthetic tests to develop an improved stacking approach and retrieved stress drop measurements with low standard deviation and reliable spatiotemporal patterns for an induced sequence in Oklahoma. Shearer et al. (2019) compared small earthquake corner frequencies estimated using a spectral ratio method (local EGF varying by earthquake) and spectral decomposition method (a single global EGF for all the earthquakes), and found the spectral ratio corner frequencies are slightly larger than those from the spectral decomposition method. They also showed that the frequency range of the Southern California regional seismic network data is insufficient to resolve source scaling and absolute values of stress drop, and

their variation, independently.

To investigate in more detail the relative effects of limited frequency range and assumptions about attenuation structure on stress drop measurements, we need an exceptionally well-recorded data set. The Parkfield segment of the San Andreas Fault in California has been densely instrumented for decades as a consequence of the Parkfield Earthquake Prediction Experiment (Bakun & Lindh, 1985), and the San Andreas Fault Observatory at Depth (SAFOD, Zoback et al., 2011). This instrumentation includes a borehole seismic network (Malin et al., 1989), that is able to record higher frequency signals than the surrounding surface networks. Allmann & Shearer (2007) performed a spectral-decomposition based study of earthquake stress drop in the region using the surface recordings. The occurrence of the 2004 M6 earthquake enabled them to look for temporal as well as spatial variation in stress drop. However, many of the earthquakes included in the analysis were relatively small (M<2) compared to the frequency range of the data available. Here we use the higher-frequency borehole recordings to perform a similar analysis, and can investigate directly the effects of using the limited frequency range of the surface data. We are also able to include data for a further decade following the 2004 M6 earthquake than the earlier study.

The large body of previous work in the region provides us with context in which to interpret our results. The seismicity is well-located (e.g., Waldhauser et al., 2004), and includes sequences of near-identical, repeating sequences (Nadeau & McEvilly, 1999, 2004). Analysis of variability in the moment and timing of these repeating earthquakes has revealed intriguing spatial and temporal variation in the stressing rate (e.g., Chen et al., 2010; Lengliné & Marsan, 2009; Nadeau & Johnson, 1998). Measurements of aseismic slip in the region have also revealed the gradual transition from creeping north-west of Middle Mountain to fully locked to the south-east of the HRSN, as well as temporal variations related to the 2004 M6 earthquake, and other events (e.g., Murray & Langbein, 2006). There have also been multiple studies of the coseismic and postseismic slip, and stress changes associated with the 2004 earthquake (e.g., Dreger et al., 2005; Jiang et al., 2021). The velocity structure (e.g., Thurber et al., 2004) and attenuation structure (e.g., Abercrombie et al., 2000; Bennington et al., 2008) are well known, and changes in both following the 2004 M6 earthquake have been observed (e.g., Brenguier et al., 2008; Kelly et al., 2013; Sheng et al., 2021). Allmann & Shearer (2007), subsequently referred to as AS2007, found spatial variations in stress drop that did not obviously correlate with other parameters, and remained relatively stable, unaffected by the 2004 M6 earthquake. They also observed temporal changes in both stress drop and attenuation following the M6 earthquake, with different regions of decrease, and increase in each, but the temporal changes in stress drop were small compared to the spatial variation. Detailed studies of individual specific repeating sequences using the borehole recordings reported a decrease in stress drop followed by recovery for some sequences, but not others (e.g., Abercrombie, 2014, 2021; Kim et al., 2016), and also increases in attenuation and recovery on a similar time scale (Kelly et

al., 2013). No large-scale analysis of the borehole recordings for earthquake source parameters has been performed to date.

We use borehole recordings and the spectral decomposition approach (Shearer et al., 2006a; AS2007; Chen & Abercrombie, 2020) to estimate stress drop for over four thousand earthquakes M0-4, from 2001-2016, in the San Andreas Fault zone at Parkfield. First, we investigate the effects of using different inversion methods, and allowing for spatial, depth, and temporal variation in attenuation and rupture velocity. We then compare the results obtained with different frequency ranges to quantify the effects of the limited bandwidth that is typically available for studies using surface recordings. Finally, we interpret our preferred results of spatial and temporal stress drop variation in the context of existing observations of the structure, and distribution of seismic and aseismic slip on the fault.

2 Data

We select our study area as an 80 km section of the San Andreas Fault centered on the shallow borehole High Resolution Seismic Network (HRSN, Karageorgi et al., 1992; Malin et al., 1989). This includes parts of the 'creeping zone' to the northwest and the 'locked zone' to the southeast of Parkfield (Harris & Segall, 1987; Murray & Langbein, 2006). We download the triggered vertical-component waveforms at the 13 HRSN stations for all the earthquakes in the Northern California double-difference catalog (WNC catalog, Waldhauser, 2009; Waldhauser & Schaff, 2008), from Northern California Earthquake Data Center (NCEDC), see Figure 1). We include only earthquakes between 2001 and 2016 (the time of our download); the recording system was less consistent before 2001, with more frequent recording system changes and lower dynamic range (which caused clipping of large earthquake records). The waveforms have sampling rate of 250 Hz and we apply the corrections for gain changes included in the instrument response table at the NCEDC. We use P wave phase picks in the NCEDC database, and use an STA/LTA based auto-picker (Li & Peng, 2016) to determine automatic picks for any waveforms without catalog arrival times.

We calculate the P-wave displacement spectra required for our analysis, using 1-second time windows, starting 0.1 s before the P wave arrival pick (see example in Figure S1). We compute the multi-taper spectral density and convert the recorded velocity spectra to displacement spectra. There is no need to correct for the instrument responses as these are included in the site terms in the spectral decomposition analysis. We also calculate the noise spectra using 1-second windows immediately preceding the signal windows, following the same approach. We select the earthquakes with sufficiently high-quality recording for the spectral analysis. We require an earthquake to be recorded by at least 5 stations, each with signal-to-noise ratio (SNR) higher than 10 at each frequency point between 2 and 60 Hz. The 4537 earthquakes between Mw0 and Mw4 that meet our data selection criteria are shown in Figure 1.

3 Theoretical Background and Spectral Decomposition Analysis

Method

3.1 Spectral decomposition to obtain relative event source spectra

To measure the source parameters, we need to isolate the source contribution from the other effects within the recorded earthquake waveforms. An observed waveform (Figure S1) can be represented as the convolution:

$$S(t) = \mathrm{ET}(t) * \mathrm{ST}(t) * \mathrm{PT}(t) \tag{1}$$

where ET, ST and PT refer to the event term, site (or station) term and path term, respectively, all functions of time (t). Transforming Equation 1 to the frequency domain, and taking the logarithm converts the equation into a linear system that can be solved iteratively for ET, ST and PT as functions of frequency, following the Spectral Decomposition method developed by Shearer et al., (2006a) using a large number of earthquakes and stations:

$$S(f) = \mathrm{ET}(f) + \mathrm{ST}(f) + \mathrm{PT}(f) + R(f) \tag{2}$$

where $R(f)$ is a residual term from the solution of the overdetermined equations. However, spectral decomposition only obtains the relative shape of the source spectra, and an additional correction is required to remove any site effects that are common to all events.

After calculating the event spectra ($ET(f)$, which can be considered relative source spectra), we follow Shearer et al. (2006a) to calculate the relative seismic moment of each event assuming it is proportional to their low frequency (2-4 Hz) amplitudes. To convert these relative moment estimates to actual moments and moment-magnitudes, we calculate their relationship with the catalog (Waldhauser & Schaff, 2008) local magnitudes. We observe a linear relationship for events with either ML 1.40 or ML<=0.83, but an excess of events with ML~1 (Figure S2). We therefore exclude these ML~1 earthquakes from the calibration. We calculate the best fitting linear relationship for events with ML 1.40 and ML<=0.83, and assume that ML = Mw when ML = 3.0 (Shearer et al., 2006a; AS2007) to derive moment estimates for all earthquakes in our dataset. The linear relationship has a slope of 0.92, consistent with previous studies of earthquakes in this magnitude range that typically find values of about 1 (e.g., Abercrombie, 1996; Ben-Zion & Zhu, 2002; Hanks & Boore, 1984), smaller than the 1.5 assumed for larger earthquakes in the original definition of Mw (Kanamori, 1977).

Estimating the actual source spectra from the event terms requires either an assumption of a reference site (e.g., *Bindi et al., 2020; Oth et al., 2011*), or a source model (Shearer *et al.*, 2006a) to correct for higher frequency attenuation and amplification effects. We follow the approach of Shearer et al. (2006a),

calculating empirical correction spectra (ECS) to extract estimates of the absolute source spectra. The basic Spectral Decomposition approach also assumes a simplified attenuation structure in which *PT(t)* depends only on the travel time. Any spatial variation in attenuation, including a dependence on source depth (as observed by Bennington et al., 2008) is not included, and will be absorbed into the event term and bias the resulting source spectra (e.g., Shearer et al., 2019; Abercrombie et al., 2020). In other words, ET(t) in equation (1) will include both the real source term and a function that includes common effects at all events and all sites, and source region specific attenuation. We investigate the effects of this assumption, and whether it is possible to address its effects by comparing a single ECS for the entire data set with separately calculated ECSs for different spatial source regions. Tomography models have shown strong spatial variations of material properties in the study region (e.g., Bennington et al., 2008; Thurber et al., 2004; Thurber et al., 2006; Zeng & Thurber, 2019; Zhang et al., 2007). We search for the most appropriate strategy that allows us to remove the influence of heterogeneous attenuation on stress drop estimations while maintaining an adequate number of events for stable stacking analysis.

3.2 Calculation of stress drop from earthquake source spectra

To calculate the source spectra, source parameters and the empirical correction spectra, we assume that the earthquake far-field displacement spectrum can be described by a Brune-type source model (Brune, 1970):

$$s(f) = \frac{M_0}{1 + \left(\frac{f}{f_c}\right)^n} \tag{3}$$

where f_c is the corner frequency, and n is high-frequency fall-off rate, which we set to 2 (ω^{-2} model). Some studies have allowed the fall-off rate to vary, but found that it can tradeoff with the corner frequencies (e.g., Shearer et al., 2019; Trugman & Shearer, 2017; Ye et al., 2013) and so we choose to fix it here.

Assuming simple circular rupture, the corner frequency (f_c) can be used to calculate the source radius (Brune, 1970; Madariaga, 1976):

$$f_c = k\frac{\beta}{r} \tag{4}$$

where β represents the shear velocity, and k is a constant that depends on model assumptions, such as the source geometry, and rupture velocity (Kaneko & Shearer, 2014, 2015). We choose k=0.32 for P waves from Madariaga (1976), which is consistent with AS2007, and Kaneko & Shearer (2015). The dependence on β introduces a dependence on depth, since β is depth dependent. For example, if rupture velocity is assumed to be a constant fraction of β then depth varying velocity should be used. If a constant β is assumed in equation (4) for all depths,

then this can also introduce an artificial dependence of source parameters on depth (e.g., Allmann & Shearer, 2007).

The earthquake stress drop (σ) can then be calculated from the seismic moment (M_0) and the source radius (r) following Eshelby (1957):

$$\sigma = \frac{7}{16}\left(\frac{M_0}{r^3}\right) = M_0\left(\frac{f_c}{0.42\beta}\right)^3 \tag{5}$$

The stress drop derived from spectral fitting must be considered an approximation. Theoretically it is related to the dynamic properties of the earthquake based on a circular rupture model assumption (Brune 1970; Madariaga, 1976), differing from the "static stress drop" derived from finite slip source parameters (e.g., Noda et al., 2013). In practice, it may be closer to a static stress drop since it is essentially the ratio of the slip to an approximation of the source dimension.

3.3 Stacking method to obtain an Empirical Correction Spectrum (ECS)

We use an adaptation of the stacking method developed and used by Shearer et al. (2006a) and AS2007 to invert the event spectra for a source model, source parameters and an empirical Correction Spectrum (ECS). Shearer et al. (2006a) stacked the event spectra into small Mw bins, and then inverted for a single ECS common to all events included in the stack and the best fitting stress drop common to all stacked M ranges, assuming the Brune (1970) source model. They also used the same approach to calculate an ECS for each event based on the 200 nearest neighbors, which involves variable spatial averaging due to the variability of the seismicity distribution; AS2007 used the latter approach. Trugman & Shearer (2017) also inverted for a common ECS, and allowed for a Mw dependence of stress drop. Shearer et al. (2019) showed that this Mw dependence may not be resolvable with many data sets, finding strong trade-offs among the scaling factor, spectral fall-off rate, and reference stress drops.

Here, we follow a modified stacking approach proposed by Chen & Abercrombie (2020), known as SNSS (Stacking-No-Self-Similarity assumption) to fit the stacked event spectra and solve for the ECS and mean stress drop. The SNSS approach does not include any assumption about stress drop scaling with magnitude, but inverts for the best fitting ECS common to all bins, while allowing the stress drop in each magnitude bin to vary independently. Chen & Abercrombie (2020) developed a series of synthetic experiments to validate the SNSS approach, and found that it performed better than the original stacking approach. They were unable to test approaches that simultaneously solve for scaling factors, because synthetic experiments indicated that their data set was too limited, with too much inter-event variability to resolve a scaling factor.

We calculate stacked spectra for each calibrated magnitude bin from Mw0.9 to Mw4.0 in increments of 0.3 M units of calibrated magnitudes. Chen & Abercrombie (2020) found that the SNSS approach can recover the true input stress drop when the corner frequency of the lowest magnitude bin is within 80% of the upper limit of the frequency range of the data. This implies that for the upper frequency limit of 60 Hz in this study, the lowest magnitude bin should have a corner frequency of 48 Hz or lower for unbiased stress drop estimation. Assuming the average stress drop about 6 MPa determined by AS2007, the estimated corner frequency of Mw=0.9 (the smallest magnitude bin that is well recorded) would be 75 Hz, Mw=1.2 would be 53 Hz, and Mw=1.5 would be 38 Hz; thus the corner frequency of the Mw0.9 bin, is too high to constrain in the inversion. Based on these estimations, we combine the SNSS and the fixed-stress drop approach in Baltay et al. (2010) to develop a hybrid-adaptive approach that enables us to include the large number of earthquakes in the Mw0.9 bin, but constrain the inversion with larger Mw events. We first apply the SNSS approach to magnitude bins with Mw 1.5 to obtain the best-fitting reference stress drops for the Mw1.5 bin. Then we fit the stacked event spectra in the Mw0.9 bin fixing the stress drop to the value we obtain for the Mw1.5 bin, to calculate an ECS following Baltay et al., (2010). We refer to this modified approach as the Self-Adaptive SNSS method (but still abbreviate it as SNSS in this study for simplification). This hybrid approach has the advantage of obtaining unbiased stress drop values that are specific to the dataset, instead of an assumed global average value as in Baltay et al. (2010), while also including solutions for small earthquakes and an estimation of ECS from the magnitude bin with most abundant earthquakes.

To calculate actual source parameters, each individual event spectrum is corrected using the common ECS determined from the SNSS inversion, and then fit using the selected source model and assumed constants. We perform a comparison of the original method of Chen & Abercrombie (2020) with our new hybrid SNSS method using a spatially compact dataset with 220 earthquakes, and find generally consistent results. The new method leads to lower magnitude scaling (Figure 2), as a consequence of the different ECS in the two methods, most likely representing the well-known increasing uncertainties and trade-offs as the corner frequency approach the limits of the frequency range of the recorded signal (e.g., Abercrombie, 2015; Ruhl et al., 2017). but there is no solid evidence of how the change compares to the magnitude scaling due to frequency band limitation, or if lower magnitude scaling means more accurate stress drop estimation.

4 Spectral Analysis of the Parkfield dataset

To investigate the effects of different assumptions about source model, and spatial and temporal variation in path effects (and ECS), we perform a sequence of independent inversions. All of these start from the event spectra calculated in the single spectral decomposition inversion of the entire dataset. We first investigate the effects of spatial binning only, using the entire data set, and then

separate the earthquakes into 3 time intervals related to the 2004 M6 earthquake to investigate temporal variation.

4.1 Initial single bin inversion (Strategy 1)

First, we perform a single inversion of all the event spectra to solve for stress drops for all individual earthquakes in our dataset. We use the hybrid SNSS approach to calculate a single ECS to correct for the source spectra of all the earthquakes (no consideration of spatial varying attenuation), and use a constant shear wave velocity (assuming constant rupture velocity) to compute stress drops from corner frequencies and moments with Equation 4 (Figure 3).

To quantify any dependence of stress drop on seismic moment, we calculate the median stress drop in overlapping Mw bins of 1 Mw unit width centered at 0.5 unit intervals. We then use linear regression to find the best fitting trend and R-squared value (squared correlation coefficient) in two separate intervals with a relatively large number of events: (i) Mw0.75-1.75, in which stress drop increases with moment, and (ii) Mw1.75-2.75, in which there is negligible dependence of stress drop with moment, see Table 1 and Figures 3B and S6.

We use a similar approach to quantify any dependence of stress drop on depth, by calculating the median stress drop in 1 km depth intervals. The results of the single inversion with no correction for depth dependent velocity or attenuation indicate an increase in stress drop with depth, both between 1.5 and 6.5 km, and between 6.5 and 11.5 km (Table 1 and Figure 3A).

4.2 Spatial Variation: With Depth and Along Strike

4.2.1 Single bin, constant shear wave velocity ( ) or variable ? (Strategy 2)

To investigate the effects of allowing for a depth-varying rupture velocity, proportional to the shear wave velocity, we compute stress drop using the same corner frequencies from the single inversion (Strategy 1), but use the shear wave velocity from the 1D velocity model (Figure S3) used by AS2007, based on the Thurber et al. (2004). Table 1 and Figure 3 show that the magnitude dependence is slightly weaker between Mw0.75 and Mw1.75, and the depth dependence is significantly weaker than when no depth dependence to velocity was included (Strategy 1), demonstrating the importance of velocity correction in stress drop estimations. We do not apply any lateral velocity correction because of the significantly smaller velocity variation along strike than with depth (Thurber et al. 2004). Also, because our event terms are obtained from all stations, on both sides of the fault, we cannot easily consider the velocity differences across the fault. To do so would require separate spectral decomposition for the stations on each side of the fault (for which we have insufficient stations and earthquakes), and so we simply use an average velocity structure with depth here.

4.2.2 Effect of Depth Bins, constant or Variable (Strategies 3 and 4)

To investigate the effects of allowing the ECS to vary with depth, and account for possible variation in attenuation with depth, we divide the dataset into four depth bins (1-4, 4-5, 5-8 and 8-15km) guided by the velocity structure (Figure S3) and earthquake distribution, ensuring sufficient earthquakes within each bin for a stable inversion. We repeat the analysis both assuming a constant shear wave (and rupture) velocity (Strategy 3) and allowing shear wave velocity to vary with depth (Strategy 4). The results are compared to those in the previous inversions in Figure 4 and Table 1.

At shallower depth, the depth-dependence of stress drop is significantly reduced by using variable (slope reduces by 60% comparing Strategy 3 and 4), but only slightly reduced with only depth-dependent attenuation (slope only reduces by 22% comparing Strategy 1 and 3). However, at deeper depth, the depth-dependent attenuation correction has significant impact on the depth-dependence of stress drop (slope reduction of 85% between Strategy 1 and 3). Slopes of magnitude dependence are also reduced, albeit slightly.

4.2.3 Effect of Spatial Bins, constant or Variable (Strategies 5 and 6)

To determine a reasonable along-strike spatial bin size to use, we first perform a simple test to compare results of increasing sized spatial bins. Smaller bins allow for greater resolution of spatial variability, and are closer to the assumptions of the underlying EGF approach (e.g., Abercrombie, 2015), but in the stacking approach, it is the large number of earthquakes included (e.g., at least 200 as used in AS2007) that provides stability. If the spatial bin size is too small, the number of events will be inadequate to obtain a stable ECS; if the bin size is too big, the spatial variation in ECS will be insufficient to account for heterogeneity.

We select 3 different bin sizes (1x1 km^2, 5x1 km^2 and 10x1 km^2, along-strike between 20 and 30 km, and at 4-5 km depth) from a part of the fault with sufficient earthquakes for stable inversion (Figure 4). We use a narrow depth range to minimize the effects of depth dependence in this test. The three bins include 350, 1100, and 1400 earthquakes respectively, and the smaller bins are subsets of the larger bins. We solve for ECS and source parameters within each bin separately, and then compare the results for common events (that is, the 350 events in the 1km bin).

We find that the ECS from the three spatial bins are almost identical with only minor deviations from the 1 km bin (Figure 4), and the corner frequencies and stress drops are nearly identical for the common earthquakes from bins with different sizes. Only minor deviations occur when the corner frequency approaches or exceeds the frequency limit of the data. This comparison suggests that ECS can be assumed to be constant within a 10 km along-strike bin size to resolve earthquake source parameters. This 10 km bin size is large enough that there are enough earthquakes in most bins to apply the stacking analysis with both along strike and depth varying ECS.

Based on this test, we adopt the following preferred spatial binning strategy:

(1) split the 80km long along-strike fault section into 8 along-strike bins of 10 km;

(2) split the along-strike bins into 1-4, 4-5, 5-8 and 8-15km depth bins (i.e., the same as depth ranges used in Strategies 3 and 4, Section 2.2.2);

(3) only invert spatial bins containing at least 200 events to guarantee enough earthquakes above Mw>0.9 (Figure S4).

We also compare the performance of the original SNSS in Chen & Abercrombie (2020) with the new hybrid SNSS in Figure S5. We repeat the analysis both assuming a constant shear wave (and rupture) velocity (Strategy 5) and allowing shear wave velocity ( ) to vary with depth (Strategy 6). The results are compared to those in the previous inversions. We note that the spatial bins further reduce the magnitude dependence between Mw0.75 and Mw1.75 with slopes reduced to 0.384 and 0.354 with constant and variable , respectively (Table 1). The depth dependence does not change significantly compared to simple 1-dimensional depth binning (Strategies 3 and 4).

4.2.4 Summary of effects of spatial attenuation and velocity corrections in stress drop calculation

Figure 3 compares the results of our inversions to investigate the effects of spatial binning (with depth and along-strike) and varying rupture velocity on the separation of source and path effects in the Parkfield region. The relatively wide frequency range of the borehole data compared to previous spectral decomposition studies provides improved resolution of source from the path and site effects. Figure 5 shows the distribution of stress drops obtained using each strategy. Not surprisingly, the largest effects are on the depth dependence of the resulting stress drop estimates, but the magnitude dependence is also affected.

Including a depth-dependent attenuation correction (Strategy 3) significantly reduces both the magnitude and depth dependence, and the standard deviation of the resulting stress drops (Figure 5) compared to Strategy 1. The finer scale lateral binning of Strategy 5 (10 km along-strike binning) only slightly reduces the dependence and standard deviation of Strategy 3 (no along-strike binning), suggesting that along-strike variation in attenuation is less significant that with depth in the study area.

The comparisons between Strategies 6 and 5, between 4 and 3, as well as between 2 and 1, show that velocity correction also significantly reduces the dependence of the calculated stress drops on both magnitude and depth.

The variation in velocity has more effect at shallow depths, where the velocity is increasing rapidly with depth, than deeper, where it is changing more slowly. Conversely, the ECS correction has a larger effect at greater depths, implying that the difference in path effects continues to be significant in this depth range.

The ECS attenuation correction and velocity corrections also have different effects on the magnitude and depth dependence of stress drops. From Table 1 and

Figure 4, magnitude dependence is more significantly reduced by improved attenuation corrections than depth-dependent velocity correction, while for depth dependence, the influence of velocity correction is more significant. AS2007 also found that depth dependence in stress drop is sensitive to the assumed velocity structure, and did not resolve any significant increase in stress drop with depth. They also found no dependence of stress drop on magnitude in a similar range to this study.

Figure 6 compares the empirical correction spectra (ECS) obtained, showing greater variability with depth than along strike, consistent with the effects on stress drop. These spatial-bin specific ECS correct for site effects common to all events. They also attempt to correct for the difference between the average regional travel-time dependent path terms from the original spectral decomposition, and the real, along path attenuation that depends on the individual source and station locations. It is hard to interpret the ECS in terms of absolute attenuation, but their differences do provide quantitative information about the variability in attenuation for earthquakes in different source locations. We fit the slopes of ECS spectra between 20 and 60 Hz, following Anderson & Hough (1984), to quantify the variability of t* in different depth ranges, and along strike (Figure 6).

As we apply increased correction for spatial variation of velocity and attenuation, the standard deviations progressively decrease from 0.66 for Strategy 1 to 0.41 for Strategy 6 (Figure 5a), implying that the variability in stress drop in an earthquake population strongly depends on data processing, and trades-off with attenuation and velocity corrections. Meanwhile, we calculate the root mean square (RMS) of the misfits between ECS and individual source spectra by frequency sample for Strategy 2, 4 and 6, and find that the median RMS of misfits from the 3 strategies synchronizes with the drop of stress drop standard deviations, which suggests that the proposed corrections may lead to better spectral fitting; however, by introducing the corrections we also introduce more free parameters that trade-off with the misfits.

4.3 Temporal attenuation correction

The 2004 M6 earthquake caused temporal changes in both the velocity and attenuation structure at Parkfield (Kelly et al., 2013; Brenguier et al. 2008; Sheng et al., 2021). To investigate any temporal variation in stress drop, we need to ensure that we are not just misinterpreting temporal variation in attenuation and other path and site effects. Hence, following AS2007 and Abercrombie et al. (2020), we divide the dataset into distinct time periods and calculate separate inversions for each. To balance the number of earthquakes needed for stable inversion, and the temporal dependence of the observed changes, we divide our dataset into three time periods (Figure S6): (1) before 2004 M6 earthquake; (2) one year following the M6 earthquake (Sep. 2004 - Sep. 2005), the approximate duration of significant attenuation and velocity changes; (3) after September 2005. We then repeat the first four different strategies used in our analysis of spatial variation. We refer to them using the same numbering, with the

additional note of being temporally corrected. The first time period, before the M6 2004 earthquake has the fewest earthquakes, and so the ECS and resulting source parameters for all spatial bins in this time interval are consequently the least well resolved (Figure S7). We do not make any temporal corrections for changes in velocity because they are too small (~0.25%, Brenguier et al., 2008; Sheng et al., 2021) to have any significant affect within our resolution and uncertainties.

There are insufficient earthquakes to divide them both along strike and into different temporal ranges for Strategies 5 and 6. We take advantage of the coherent ECSs for spatial bins of the same depth range, and adopt a hybrid-approach to combine temporal corrections and the finer-scale spatial binning for Strategies 5 and 6. First we calculate the difference between the ECS in different time periods in each depth bin, then apply these relative temporal differences to the respective ECS for the spatial bins calculated for the entire time period (Section 4.2.3) to obtain "pseudo-" temporal ECSs for each grid during each time period. Finally, we solve for the source parameters for each earthquake using the corresponding ECS based on occurrence time and location. We refer to these, our preferred, parameters as Strategy 6, with temporal correction.

Figure 5 shows the minimal effect of the temporal attenuation correction on the distribution of stress drops obtained using the different strategies. We suspect this is partly related to the increased uncertainty in the inversions, due to the smaller numbers of events in each one, offsets the increased number of free parameters. The inversions with and without temporal binning have very similar median stress drops, and reveal similar behavior of stress drop with respect to depth and magnitude (Table 1 and Figure S7).

Figure S8 shows the ECS changes for each depth bin for the three time periods, with higher amplitudes of ECS indicating lower attenuation (see supplementary text S1). We quantify the relative change in attenuation with time following the approach mentioned above. From Pre-2004 to 2004-2005, the overall ECS amplitude decreases slightly for 1-4 km (t* increase of 0.05ms) and more significantly for 4-5 km, 5-8 km and 8-15 km (t* increases of 1.75ms, 0.84ms and 0.75ms, respectively). From 2004-2005 to Post-2005, we see the reverse behavior, with the overall ECS amplitude increasing and t* decreasing by 0.18ms (1-4 km), 0.30ms (4-5 km), 1.20ms (5-8 km) and 0.32ms (8-15 km). The t* variations suggest increased attenuation immediately following the 2004 M6 earthquake, and gradual recovery over long term, which is consistent with previous studies of attenuation changes (e.g., Kelly et al., 2013). Figure S9 shows individual event corner frequencies before and after temporal correction has an average ratio of 1.011 with standard deviation of 0.34, suggesting the influence of temporal correction is relatively small.

5 Results and Discussion

We calculate stress drop for earthquakes at Parkfield using a variety of different approaches to correct for spatially and temporally varying material properties,

in an attempt to resolve the real spatial and temporal variation in earthquake sources. We use the shallow borehole (HRSN) recordings, and only include earthquakes recorded by at least 5 stations with high signal to noise ratio over the frequency range 2-60 Hz; this is a relatively wide frequency range compared to many previous spectral-decomposition studies (e.g., AS2007; Trugman, 2020; Trugman & Shearer, 2017). We apply the self-adaptive SNSS method, that does not assume any magnitude scaling, to calculate the empirical correction spectra (ECS) and isolate the source spectra. We compare our results to those of recent studies of stress drop at Parkfield including the large-scale study of AS2007 and the smaller scale analysis of Abercrombie (2014). We begin by discussing the trends, resolution and uncertainties in the data set as a whole, and then consider the spatio-temporal patterns and their reliability.

5.1 Separation and resolution of source and path effects

Perhaps the most challenging problem with obtaining earthquake source parameters is to separate the source from the path and site effects. We apply a series of data processing strategies to improve the robustness of stress drop estimation. Our resolution benefits from the relatively low noise, and wider bandwidth of the borehole stations compared to the previous similar style analysis by AS2007. This can be seen in the lower standard deviation for stress drop variability we obtain for each of our Strategies, compared to the earlier study by AS2007 (Figure 5). We find that the assumptions and choices involved in both the attenuation and velocity corrections can lead to apparent magnitude or depth dependence (Figure 3). The final preferred strategy, which includes both factors, results in the least stress drop dependence and the lowest standard deviation of stress drop variability. AS2007 used a spatially varying ECS, with the spatial smoothing depending on the local density of seismicity, and also found no resolvable magnitude or depth dependence to their stress drop values. As in most previous studies of stress drop, we observe that the standard deviation gradually increases with decreasing magnitudes. The standard deviation increases from <0.1 (for Mw 2.8) to 0.24 (for Mw 1), but even the smallest magnitude bin in this study has lower standard deviation than the largest magnitude bin in AS2007, implying a more well-constrained inversion and better parameter resolution (Figure 8). This confirms that a borehole network with wider frequency bandwidth, lower noise, and less attenuated signals can retrieve better measurements of source parameters for small earthquakes.

The standard deviation in stress drop in the entire data set decreases significantly with increasing allowance for depth dependence of attenuation and rupture velocity, implying that these factors contribute to the apparent variability of stress drop. Comparison of the empirical correction spectra shows decreasing attenuation with depth, consistent with the increase in velocity and Q with depth previously observed in the region (e.g., Thurber et al., 2004; Bennington et al., 2008). These previous analyses also find that the along strike variation is less than that with depth, again consistent with our results. Unfortunately, because the spectral decomposition approach combines stations from all azimuths

and distances, we cannot investigate any difference in attenuation across the fault.

5.2 Frequency range and Magnitude range of reliable parameters

Previous work has shown that the limited frequency range of the earthquake spectra available for modeling can significantly bias the resulting estimates of corner frequency. For example, Shearer et al. (2019) showed that the frequency bandwidth of regional Southern California Seismic Network data (~2-20 Hz) is inadequate to distinguish between different source models and scaling, and Abercrombie (2015) showed how decreasing frequency range biased the results in empirical Green's function analysis. Here our relatively wide frequency range (2-60 Hz), larger than almost all previous spectral decomposition studies provide increased resolution.

To further explore the influence of the frequency band on corner frequency estimations, and guide our interpretation of our new results, we repeat our analysis limiting the frequency range to first, 2-20 Hz and second, 2-40Hz. Figure 7 (a, b) shows that corner frequencies calculated with a narrower frequency band are much more scattered than those with a wider frequency band, especially when the corner frequency exceeds the upper limits. In addition, higher corner frequencies are systematically underestimated when using a lower maximum data frequency (Figure 7c). Previous work using an empirical Green's function approach by Abercrombie (2015), Abercrombie et al. (2017) and Ruhl et al. (2017) found that systematic low bias in corner frequency estimates starts at a half or two thirds of the maximum frequency of the data. Chen & Abercrombie (2020) found similar results using spectral decomposition, although their synthetic tests suggested that sometimes corner frequencies of 80% the maximum frequency could be resolved using the SNSS approach. In Figure S5 we show that our new hybrid SNSS approach somewhat mitigates the problem compared to the original SNSS approach in Chen & Abercrombie (2020); in the hybrid approach the smallest magnitude bin have stress drop derived from the largest magnitude bins that is used to calculate the empirical correction spectra. We still observe increased variability at smaller magnitudes, probably largely reflecting increased uncertainties, but we see less systematic bias.

AS2007 used surface stations and a narrower frequency range in their analysis, the narrower frequency range being a direct consequence of the near-surface attenuation and higher noise in the surface recordings. It is likely that the lower frequency bandwidth is causing the higher standard deviation and the lower median values reported by AS2007, compared to the current analysis (Figure 5 and 7). Figure 7d shows a constant shift of approximately a factor of 1.2 when compared to our preferred, full bandwidth results. This translates to approximately 1.7 times (1.2^3) difference in stress drop, consistent with the difference of the median stress drop values in these two studies; we obtain ~10MPa for the borehole dataset, while AS2007 report ~6MPa using similar constants in equation 5. In Figure 7c we see that the AS2007 corner frequencies are lower than those from our analysis using the same (2-20 Hz) frequency range. This

suggests that the more attenuated surface data may tend to underestimate the stress drop during the ECS calculation, although the random uncertainties are also large from such a limited range (e.g., Shearer et al., 2019).

In all analyses shown in Figure 7, some events with corner frequencies near the limits of the data can be very high, or low. This is possibly due to a combination of the effects of limited bandwidth with complexity in the earthquake sources themselves, that is ignored in the simple spectra fitting. Abercrombie (2021) demonstrates how this can bias the results, especially for particularly complex events, and Yoshimitsu et al. (2019) also note how the inappropriateness of the simple Brune source model individual earthquakes greatly increases the uncertainties of stress drop estimates.

Given the above discussion, Mw1.5 is the lowest magnitude for which we should be able to resolve corner frequency without bias using our approach, given the maximum signal frequency of 60 Hz and a reference stress drop of 10 MPa. In practice, we find that the median stress drop of the M>1.1 earthquakes (median $\log_{10}(\Delta) = 1.24$) is not significantly different from that of the M>1.5 events (median $\log_{10}(\Delta) = 1.32$), given the standard deviation of the whole data set (0.43). We also compare the spatiotemporal variations of stress drop with different magnitude cutoffs in Figure S10, and find that patterns with M>1.1 is similar to higher magnitude cutoffs, therefore, we include earthquakes with M>1.1 in our interpretations.

5.3 Implications for stress drop scaling with depth and magnitude

We find that including reasonable corrections for depth dependent attenuation and rupture velocity can remove all need for any systematic dependence of stress drop on source depth in the upper 15 km at Parkfield. This is consistent with the previous results of AS2007. It is also in agreement with a recent meta-analysis (Abercrombie et al., 2020) that showed that previously reported increases in stress drop with depth could potentially be artefacts of inadequate correction for depth dependent path effects.

Less intuitively, improving corrections for depth variation in attenuation and velocity also decreased the resulting magnitude dependence of the stress drop results. The magnitude dependence is weak to the point of negligible above M1.75, but at lower magnitudes, some increase in stress drop with magnitude remains, regardless of correction strategy (see Figures 3, S6 and Table 1). We also observe increased variability at smaller magnitudes (Figure 8), probably largely reflecting increasing uncertainties. Based on previous analysis of the effects of frequency bandwidth limitations (e.g., Abercrombie, 2021) and our own analysis discussed above, we interpret this is a resolution effect, rather than a real physical effect.

5.4 Spatiotemporal variability of stress drop and the effects of the 2004 M6 Earthquake

Figure 9 shows the stress drop spatial variations in 3 time periods: 1) Mar 2001 –

Sep 2004, 2) Sep 2004 – Sep 2005, and 3) Sep 2005 – Aug 2016, projected onto the San Andreas Fault. We smooth the distribution by dividing the study area into 4 km (along strike) by 2 km (along depth) grids, and obtain the median stress drop for grids with more than 5 earthquakes. Here we use the results for Strategy 6 (including corrections for both spatial and temporal attenuation, and depth-dependent velocity) and use earthquakes with M>1.1. The relatively small number of earthquakes in time period 1 (before the 2004 M6 earthquake) limits the spatial resolution in that time period. We also calculate a comparable figure using the results of Strategy 6, without temporal variation (Figure S11) and observe very similar patterns, suggesting that the results are not significantly affected by uncertainties in the temporal corrections.

From Figure 9, we observe considerable small-scale heterogeneity, but general stability and consistency over the entire time period. AS2007 also observed no significant change in the spatial distribution before and after the 2004 M6 earthquake. We infer this to indicate that the spatial variability in fault conditions is significantly larger than any temporal effects caused by the coseismic or postseismic slip. Similar spatial stability was reported by Ruhl et al. (2017) for the well recorded Mogul earthquake sequence in Nevada, as well as Uchide et al. (2014) for M3.0-4.5 earthquakes in the 2011 Tohoku earthquake area, suggesting structural or material heterogeneity is the dominant factor of stress drop variability. This is also consistent with the constant rupture directivity of sequences at Parkfield analyzed by Abercrombie et al. (2020), but contrasts with similar sized spatial and temporal variation associated a M6 earthquake on the Gofar transform fault, reported by Moyer et al. (2018).

Also in Figure 9, we observe no clear difference between the stress drop distribution in the locked and creeping parts of the fault. Inversions by Murray & Langbein (2006) indicate that above about 15 km depth, NW of the 1966 hypocenter, the fault is essentially creeping throughout this time period, and to the SE it is primarily locked, slipping seismically and post-seismically in 2004 to 2005. This division is not visible in Figure 9, suggesting that the stress drops of small earthquakes are not primarily affected by the nature of slip on the surrounding fault at large scale. These results contrast with the reported along-strike variation in stress drop of earthquakes on the Gofar oceanic transform associated with different levels of inferred seismic and aseismic slip (Moyer et al., 2018). With only two examples, we cannot draw any reliable conclusions as to why the faults may behave (or only appear to behave) differently.

We compare our observations of spatially varying stress drop to the various finite-fault inversions of the 2004 M6 earthquake (Dreger et al. 2005, Custódio et al., 2005) , but again see no clear correlation. This is partly because of variability in the different inversions which do not have resolution on the scale of the spatial heterogeneity we observe, but we see strong variation in stress drop even in regions with high slip in most models (e.g., between the 1966 hypocenter and SAFOD). Combining GPS data and seismicity, Jiang et al. (2021) observed complex multistage slip patterns, suggesting afterslip rate and local structure

controls fine-scale seismicity behaviors.

At smaller scale, we observe considerable variability, that shows some consistency and some variation from the earlier results of AS2007. Their study included more earthquakes before the 2004 M6, but also is likely to have larger uncertainties because of the lower quality of their data. The high level of small-scale heterogeneity is consistent with the observations of the behavior of repeating sequences by Lengline and Marsan (2009). It does not show any clear dependence on other known characteristics of the fault zone. For example, we observe regions of high and low stress drop around the hypocenters of both the 1966 and the 2004 earthquakes.

The temporal variations we observe in both attenuation and stress drop are relatively small compared to the spatial variations. Figure S8 shows the differences in attenuation in different depth and time periods. Figure 10 compares our observed temporal variation in stress drop, in the different time periods, to that reported by AS2007. Because of the shorter time span of AS2007 after the 2004 earthquake, we only compare the temporal changes between period 2 and period 1. For each grid used in Figure 9, we calculate the difference in average stress drop values between successive time periods (i.e., Period 2 - Period 1, and Period 3 - Period 2). Again, we use all earthquakes M>1.1; we obtain consistent results with a magnitude cut off of 1.1 or larger (Figure S10). Like AS2007, we observe regions of increase and decrease in stress drop following the 2004 M6 earthquake. The region of high slip in the M6 earthquake (according to Dreger et al., 2005) encompasses stable patches of high and low stress drop.

The increase in absolute values of attenuation at shallow depths (< 4 km), obtained here following the 2004 M6 earthquake, are almost a factor of ten smaller than those calculated from repeating earthquakes in the same depth range by Kelly et al. (2013). This may represent a combination of temporal averaging, and smoothing of small-scale heterogeneous behavior in our larger-scale analysis, or result from the uncertainties in either or both studies. Unlike Kelly et al. (2013), we observe larger temporal variation in attenuation at greater depths (5-8 km). This also contrasts with the conclusion that the larger velocity changes (~0.25%) are limited to the upper 1-2 km (Sheng et al., 2021; Wu et al., 2016). We observe a decrease in attenuation from 2005 to 2016, that is about 1/2 to 2/3 times that of the increase following the 2004 M6 earthquake. This asymmetry may indicate incomplete recovery, or simply reflect the uncertainties. Malagnini et al. (2019) investigated temporal and spatial changes in attenuation at Parkfield using coda waves, and reported variation on a range of time scales. They found that the 2004 M6 earthquake affected the attenuation variation on the NE and SW sides of the San Andreas Fault very differently. Our analysis averages the behavior of both sides of the fault.

Clearly, fully separating temporal variation in stress drop and attenuation remains a challenge, and we take this into account as we attempt to interpret out results. To discuss the complex patterns, we observe and their resolution, we focus on four regions indicated on Figures 9 and 10. Ideally, we would use

smaller regions, guided by the spatial variation, but they contain insufficient earthquakes to make reliable conclusions. We therefore choose regions thought to represent different conditions and behaviors, and explore the stress drop variations within.

Region I: SAFOD Region. We start by discussing the shallow region surrounding SAFOD as it includes repeating sequences of well-studied earthquakes that we can use to assist in assessing the reliability of our results. It is a region of fairly average stress drop values in our analysis (Figure 9). Abercrombie (2014) used an individual-event based spectral-ratio approach to obtain corner frequencies, and for earthquakes in the three sequences of earthquakes targeted by SAFOD. For the largest magnitude sequence (T1, M~2.1), the simple circular source model was a good approximation, and Abercrombie (2014) found good agreement with the results of AS2007 for the same events; both studies found that the immediately after the 2004 M6 earthquake had significantly lower stress drops than the other events. Time domain source modeling, also using empirical Green's functions, by Dreger et al. (2005), and Kim et al. (2016) also revealed a similar relative temporal behavior for the same earthquake sequence. Sequence T2 involved complex sources and was not well modeled by Abercrombie (2014). Sequence T3 is too small to be resolved in the study of AS2007, but Abercrombie (2014) observed similar decrease in stress drop for events in this sequence immediately following the 2004 M6 event, albeit with larger uncertainties. In Figure 11, we compare our results to those of Abercrombie (2014) for the same earthquakes. We see better agreement for the lower frequency measurements, but at higher corner frequencies the results of Abercrombie (2014) are systematically higher. This could be due to Abercrombie (2014) using a higher upper frequency limit for these well-recorded earthquakes (~90 Hz) or else may be method dependent (see Shearer et al., 2019; Abercrombie, 2021). Pennington et al. (2021) performed a comprehensive comparison of methods to estimate stress drop for earthquakes in the Prague, OK, 2011 sequence, and found that although the absolute values varied considerably, there was good agreement between the relatively low and high stress drop populations among the different methods and independent studies. For the better-quality results of Abercrombie (2014) in Sequences T1 and T3, we observe that both studies have relatively low corner frequencies for the events immediately after the 2004 M6, compared to the other events. This comparison gives us some confidence that we are observing real temporal variation. It is still possible that very localized, short term variation in attenuation is causing similar apparent variation in source parameters in all the studies. Certainly, the earthquake seismograms recorded shortly after the M6 event have relatively low high-frequency energy. The fact that in our work, and that of Abercrombie (2014) and Abercrombie et al. (2020), some temporal stress drop variation remains regardless of the various attenuation corrections tried, suggests that at least some of the variation in source parameters is real.

Figure 10 shows on average a small increase in stress drop in the region around SAFOD, in the year after the M6 earthquake, followed by a small decrease.

Figure 10, B1 shows the high level of variability and the changes within the one-year period we average for our Time 2. The variability implies that to identify more significant variations would require smaller scale spatial and temporal resolution than is available.

Region II: Aseismic Creep Region. This region is of interest as it is in the part of the fault thought to be almost entirely slipping aseismically (e.g., Murray & Langbein, 2006). In our analysis, it is characterized by relatively high values, but they are no higher than those around the 2004 hypocenter, and the creeping region nearer to SAFOD has lower values, negating a simple relation between high stress drop and creep (Figure 9). AS2007 observed an apparent increase in stress drop in this region, following the M6 but did not have sufficient earthquakes to resolve it. The region is just outside the HRSN network, but we observe a decrease in stress drop following the M6, and an increase afterwards. Again, these are very small trends amidst much variability (Figure 10, B2).

Region III: 1966 Hypocentral Region. This region, also known as the Middle Mountain asperity, also shows variable behavior with patches of relatively high and low stress drop. Unfortunately, the lack of events in these individual smaller regions in all time periods means that we cannot resolve time variation on this scale. The region is dominated by a decrease in stress drop (Figure 10, B3) immediately following the 2004 M6 earthquake, and then returns to normal within the year. The immediate decrease of stress drop is consistent with observations from other large earthquakes, for example, the M5.7 Prague earthquake (Yenier et al., 2017). In fact, some high stress drop events in the region near the end of time period 2 increase the average and lead to an apparent decrease in stress drop in the following time period (compare Figure 10, B3 with Figures 10, A2 and A3). In this region, Abercrombie et al. (2020) and McLaskey et al. (2012) observed one relatively well-recorded sequence to exhibit a possible decrease then gradual increase in stress drop. South of the 1966 hypocenter in this region, Jiang et al. (2021) observed significant coseismic slip and afterslip about 8 hours following the 2004 earthquake, which coincide with an area of stress drop increase (Figure 10, A2), suggesting possible influence of fault slip on stress drop changes.

Region IV: 2004 Hypocentral Region. Like the hypocentral region of the 1966 earthquake, this region shows some strong spatial variation and less clear temporal variation, with opposite changes to AS2007 (Figures 10, A1 and A2). This is largely because of the lack of events prior to the M6 earthquake. Figures 10, A2, A3 and B4 suggest that the region is dominated by a decrease in stress drop immediately following the M6, and then gradual recovery. This region experienced complex slip history with coseismic slip and afterslip featuring slip reversals and slip pulses (area R1 in Jiang et al., 2021). These complex stress changes complicate the interpretation of stress drop variations in this region.

Overall, in regions I, which is located at the shallow portion of cosesimic slip zone, we observe less coherent temporal changes in relation with the 2004 M6 earthquakes, however, individual repeating sequences exhibit robust stress drop

decrease after the 2004 event. In region II, where no significant coseismic and post-seismic slip has been reported, we observe small trend with large variability. In region III, where both significant seismic and postseismic slip are observed, clear temporal variation of stress drop is observed. Temporal variation of region IV is less resolved due to limited number of earthquakes prior to the 2004 earthquake. Observations in regions I and III suggest that fault slip influence spatiotemporal distributions of stress drop. However, amplitudes of temporal stress drop changes are relatively small compared to background stress drop spatial distributions, indicating that local fault structure is likely the major cause of spatial heterogeneity.

6 Conclusions

We use shallow borehole recordings of 4537 earthquakes at Parkfield, California, to investigate scaling, and spatio-temporal variation of stress drop. We find:

1. Correction for spatio-temporal variation in material properties is needed to improve the accuracy of stress drop estimations. In the Parkfield region, corrections for variations in attenuation and rupture velocity with depth provide the most significant improvements to the stress drop estimates.

2. The frequency bandwidth of the signal is important. Insufficient bandwidth can lead to systematic underestimation, and increased scatter of corner frequency and hence stress drop estimates. Interpretation of stress drop distributions should only include events within the resolution limit of the available dataset.

3. Apparent depth and magnitude dependence can be caused by poor correction for material properties and the limited frequency range. We see neither dependence at Parkfield.

4. At Parkfield we observe strong, stable spatial variability at small scale, with no significant dependence on the nature of fault slip (creeping versus locked) or the slip distribution of the 2004 M6 earthquake.

5. Temporal variations of stress drop following the 2004 M6 earthquake are smaller than the spatial variations, but can be observed in regions with sufficient number of events and well-resolved coseismic/post-seismic slip.

Acknowledgements

We thank Dr. Peter Shearer for sharing his ideas in the process of determining the SNSS method, and the USGS/HRSN personnel who collect and distribute Parkfield dataset online for public use (visit the USGS at https://usgs.gov for further details). Data for this study come from the High-Resolution Seismic Network (HRSN) doi:10.7932/HRSN, operated by the UC Berkeley Seismological Laboratory, which is archived at the Northern California Earthquake Data Center (NCEDC), doi:10.7932/NCEDC. Waveform data, metadata, or data products for this study were accessed through the Northern California Earthquake Data Center (NCEDC), doi:10.7932/NCEDC. Some of the computing for this

project was performed at the OU Supercomputing Center for Education & Research (OSCER) at the University of Oklahoma (OU). This project is supported by National Science Foundation (NSF) under Awards 1547071 and 1547083. The dataset used for the analysis in this research can be obtained in the first author's GitHub repository (https://doi.org/10.5281/zenodo.5129231).

References

Abercrombie, R. E. (2000). Crustal attenuation and site effects at Parkfield, California. *Journal of Geophysical Research: Solid Earth*, *105*(3), 6277–6286. https://doi.org/10.1029/1999jb900425Abercrombie, R. E. (1996). The magnitude-frequency distribution of earthquakes recorded with deep seismometers at Cajon Pass, southern California. *Tectonophysics*. https://doi.org/10.1016/0040-1951(96)00052-2Abercrombie, R. E. (2014). Stress drops of repeating earthquakes on the San Andreas Fault at Parkfield. *Geophysical Research Letters*, *41*(24), 8784–8791. https://doi.org/10.1002/2014GL062079Abercrombie, R. E. (2015). Investigating uncertainties in empirical Green's function analysis of earthquake source parameters. *Journal of Geophysical Research: Solid Earth*, *120*(6), 4263–4277. https://doi.org/10.1002/2015JB011984Abercrombie, R. E. (2021). *Resolution and uncertainties in estimates of earthquake stress drop and energy release*. *Philosophical Transactions of the Royal Society A: Mathematical, Physical and Engineering Sciences* (Vol. 379). https://doi.org/10.1098/rsta.2020.0131Abercrombie, R. E., Bannister, S., Ristau, J., & Doser, D. (2017). Variability of earthquake stress drop in a subduction setting, the Hikurangi Margin, New Zealand. *Geophysical Journal International*, *208*(1), 306–320. https://doi.org/10.1093/gji/ggw393Abercrombie, R. E., Chen, X., & Zhang, J. (2020). Repeating Earthquakes With Remarkably Repeatable Ruptures on the San Andreas Fault at Parkfield. *Geophysical Research Letters*, *47*(23), 1–10. https://doi.org/10.1029/2020GL089820Aki, K. (1967). Scaling law of seismic spectrum. *Journal of Geophysical Research*, *72*(4), 1217–1231. https://doi.org/10.1029/JZ072i004p01217Allmann, B. P., & Shearer, P. M. (2007). Spatial and temporal stress drop variations in small earthquakes near Parkfield, California. *Journal of Geophysical Research: Solid Earth*, *112*(4), 1–17. https://doi.org/10.1029/2006JB004395Allmann, B. P., & Shearer, P. M. (2009). Global variations of stress drop for moderate to large earthquakes. *Journal of Geophysical Research: Solid Earth*, *114*(1), 1–22. https://doi.org/10.1029/2008JB005821Anderson, J. G., & Hough, S. E. (1984). A model for the shape of the fourier amplitude spectrum of acceleration at high frequencies. *Bulletin of the Seismological Society of America*, *74*(5), 1969–1993.Bakun, W. H., & Lindh, A. G. (1985). The Parkfield, California, Earthquake Prediction Experiment. *Science*, *229*, 4714.Baltay, A., Prieto, G., & Beroza, G. C. (2010). Radiated seismic energy from coda measurements and no scaling in apparent stress with seismic moment. *Journal of Geophysical Research: Solid Earth*, *115*(8), 1–12. https://doi.org/10.1029/2009JB006736Baltay, A., Ide, S., Prieto, G., & Beroza, G. (2011). Variability in earthquake

stress drop and apparent stress. *Geophysical Research Letters*, *38*(6), 1–6. https://doi.org/10.1029/2011GL046698Ben-Zion, Y., & Zhu, L. (2002). Potency-magnitude scaling relations for Southern California earthquakes with 1.0 < ML < 7.0. *Geophysical Journal International*, *148*(3), F1–F5. https://doi.org/10.1046/j.1365-246X.2002.01637.xBennington, N., Thurber, C., & Roecker, S. (2008). Three-dimensional seismic attenuation structure around the SAFOD site, Parkfield, California. *Bulletin of the Seismological Society of America*, *98*(6), 2934–2947. https://doi.org/10.1785/0120080175Bindi, D., Spallarossa, D., Picozzi, M., & Morasca, P. (2020). Reliability of source parameters for small events in central italy: Insights from spectral decomposition analysis applied to both synthetic and real data. *Bulletin of the Seismological Society of America*, *110*(6), 3139–3157. https://doi.org/10.1785/0120200126Brenguier, F., Campillo, M., Hadziioannou, C., Shapiro, N. M., Nadeau, R. M., & Larose, E. (2008). Postseismic Relaxation Along the San Andreas Fault at Parkfield from Continuous Seismological Observations. *Science*, *321*(5895), 1478–1481. https://doi.org/10.1126/science.1160943Brune, J. N. (1970). Tectonic stress and the spectra of seismic shear waves from earthquakes. *Journal of Geophysical Research*, *75*(26), 4997–5009. https://doi.org/10.1029/JB075i026p04997Chaves, E. J., Schwartz, S. Y., & Abercrombie, R. E. (2020). Repeating earthquakes record fault weakening and healing in areas of megathrust postseismic slip. *Science Advances*, *6*(32), 2–10. https://doi.org/10.1126/sciadv.aaz9317Chen, K. H., Bürgmann, R., Nadeau, R. M., Chen, T., & Lapusta, N. (2010). Postseismic variations in seismic moment and recurrence interval of repeating earthquakes. *Earth and Planetary Science Letters*, *299*(1–2), 118–125. https://doi.org/10.1016/j.epsl.2010.08.027Chen, X., & Shearer, P. (2013). California foreshock sequences suggest aseismic triggering process. *Geophys. Res. Lett.*, *40*, 2602–2607. https://doi.org/10.1002/grl.50444Chen, Xiaowei, & Abercrombie, R. E. (2020). Improved approach for stress drop estimation and its application to an induced earthquake sequence in Oklahoma. *Geophysical Journal International*, *223*(1), 233–253. https://doi.org/10.1093/gji/ggaa316Custódio, S., Liu, P., & Archuleta, R. J. (2005). The 2004 Mw6.0 Parkfield, California, earthquake: Inversion of near-source ground motion using multiple data sets. *Geophysical Research Letters*, *32*(23), 1–4. https://doi.org/10.1029/2005GL024417Dreger, D. S., Gee, L., Lombard, P., Murray, M. H., & Romanowicz, B. (2005). Rapid finite-source analysis and near-fault strong ground motions: Application to the 2003 Mw 6.5 San Simeon and 2004 Mw 6.0 Parkfield earthquakes. *Seismological Research Letters*, *76*(1), 40–48. https://doi.org/10.1785/gssrl.76.1.40Eshelby JD. (1957). The determination of the elastic field of an ellipsoidal inclusion, and related problems. *Proceedings of the Royal Society of London. Series A. Mathematical and Physical Sciences*, *241*(1226), 376–396. https://doi.org/10.1098/rspa.1957.0133Goebel, T. H. W., Hauksson, E., Shearer, P. M., & Ampuero, J. P. (2015). Stress-drop heterogeneity within tectonically complex regions: A case study of San Gorgonio Pass, southern California. *Geophysical Journal International*, *202*(1), 514–528. https://doi.org/10.1093/gji/ggv160Hanks, T. C., & Boore, D. M. (1984). Moment- magnitude relations in theory and practice. *Journal of Geophysical Re-*

search, *89*(B7), 6229–6235. https://doi.org/10.1029/JB089iB07p06229Hardebeck, J. L. (2020). Are the Stress Drops of Small Earthquakes Good Predictors of the Stress Drops of Moderate-to-Large Earthquakes? *Journal of Geophysical Research: Solid Earth*, *125*(3), 1–23. https://doi.org/10.1029/2019JB018831Harris, R. A., & Segall, P. (1987). Detection of a locked zone at depth on the Parkfield, California, segment of the San Andreas fault (USA). *Journal of Geophysical Research*, *92*(B8), 7945–7962. https://doi.org/10.1029/JB092iB08p07945Huang, Y., Ellsworth, W. L., & Beroza, G. C. (2017). Stress drops of induced and tectonic earthquakes in the central United States are indistinguishable. *Science Advances*, *3*(8), 1–8. https://doi.org/10.1126/sciadv.1700772Imanishi, K., & Uchide, T. (2017). Non-self-similar source property for microforeshocks of the 2014 Mw 6.2 Northern Nagano, central Japan, earthquake. *Geophysical Research Letters*, *44*(11), 5401–5410. https://doi.org/10.1002/2017GL073018Imanishi, Kazutoshi, & Ellsworth, W. L. (2006). Source scaling relationships of microearthquakes at Parkfield, CA, determined using the SAFOD Pilot Hole Seismic Array (pp. 81–90). https://doi.org/10.1029/170GM10Jiang, J., Bock, Y., & Klein, E. (2021). Coevolving early afterslip and aftershock signatures of a San Andreas fault rupture. *Science Advances*, *7*(15), eabc1606. https://doi.org/10.1126/sciadv.abc1606Kanamori, H. (1977). The energy release in great earthquakes. *Journal of Geophysical Research*, *82*(20), 2981–2987. https://doi.org/10.1029/jb082i020p02981Kaneko, Y., & Shearer, P. M. (2014). Seismic source spectra and estimated stress drop derived from cohesive-zone models of circular subshear rupture. *Geophysical Journal International*, *197*(2), 1002–1015. https://doi.org/10.1093/gji/ggu030Kaneko, Y., & Shearer, P. M. (2015). Variability of seismic source spectra, estimated stress drop, and radiated energy, derived from cohesive-zone models of symmetrical and asymmetrical circular and elliptical ruptures. *Journal of Geophysical Research: Solid Earth*, *120*(2), 1053–1079. https://doi.org/10.1002/2014JB011642Karageorgi, E., Clymer, R., & McEvilly, T. V. (1992). Seismological studies at Parkfield. II. Search for temporal variations in wave propagation using vibroseis. *Bulletin of the Seismological Society of America*, *82*(3), 1388–1415.Kelly, C. M., Rietbrock, A., Faulkner, D. R., & Nadeau, R. M. (2013). Temporal changes in attenuation associated with the 2004 M6.0 Parkfield earthquake. *Journal of Geophysical Research: Solid Earth*, *118*(2), 630–645. https://doi.org/10.1002/jgrb.50088Kim, A., Dreger, D. S., Taira, T., & Nadeau, R. M. (2016). Changes in repeating earthquake slip behavior following the 2004 Parkfield main shock from waveform empirical Green's functions finite-source inversion. *Journal of Geophysical Research B: Solid Earth*, *121*(3), 1910–1926. https://doi.org/10.1002/2015JB012562Kwiatek, G., Bulut, F., Bohnhoff, M., & Dresen, G. (2014). High-resolution analysis of seismicity induced at Berlín geothermal field, El Salvador. *Geothermics*, *52*, 98–111. https://doi.org/10.1016/j.geothermics.2013.09.008Lengliné, O., & Marsan, D. (2009). Inferring the coseismic and postseismic stress changes caused by the 2004 Mw = 6 Parkfield earthquake from variations of recurrence times of microearthquakes. *Journal of Geophysical Research: Solid Earth*, *114*(10), 1–19. https://doi.org/10.1029/2008JB006118Li, Z.,

& Peng, Z. (2016). An automatic phase picker for local earthquakes with predetermined locations: Combining a signal-to-noise ratio detector with 1D velocity model inversion. *Seismological Research Letters*, *87*(6), 1397–1405. https://doi.org/10.1785/0220160027Madariaga, R. (1976). Dynamics of an expanding circular fault. *Bulletin of the Seismological Society of America*, *66*(3), 639–666. Retrieved from http://bssa.geoscienceworld.org/content/66/3/639.abstractMalagnini, L., Dreger, D. S., Bürgmann, R., Munafò, I., & Sebastiani, G. (2019). Modulation of Seismic Attenuation at Parkfield, Before and After the 2004 M6 Earthquake. *Journal of Geophysical Research: Solid Earth*, *124*(6), 5836–5853. https://doi.org/10.1029/2019JB017372MALIN, P. E., BLAKESLEE, S. N., ALVAREZ, M. G., & MARTIN, A. J. (1989). Microearthquake Imaging of the Parkfield Asperity. *Science*, *244*(4904), 557–559. https://doi.org/10.1126/science.244.4904.557Mayeda, K., Gök, R., Walter, W. R., & Hofstetter, A. (2005). Evidence for non-constant energy/moment scaling from coda-derived source spectra. *Geophysical Research Letters*, *32*(10), 1–4. https://doi.org/10.1029/2005GL022405McLaskey, G. C., Thomas, A. M., Glaser, S. D., & Nadeau, R. M. (2012). Fault healing promotes high-frequency earthquakes in laboratory experiments and on natural faults. *Nature*, *491*(7422), 101–104. https://doi.org/10.1038/nature11512Molkenthin, C., Scherbaum, F., Griewank, A., Leovey, H., Kucherenko, S., & Cotton, F. (2017). Derivative-based global sensitivity analysis: Upper bounding of sensitivities in seismic-hazard assessment using automatic differentiation. *Bulletin of the Seismological Society of America*, *107*(2), 984–1004. https://doi.org/10.1785/0120160185Moyer, P. A., Boettcher, M. S., McGuire, J. J., & Collins, J. A. (2018). Spatial and Temporal Variations in Earthquake Stress Drop on Gofar Transform Fault, East Pacific Rise: Implications for Fault Strength. *Journal of Geophysical Research: Solid Earth*, *123*(9), 7722–7740. https://doi.org/10.1029/2018JB015942Murray, J., & Langbein, J. (2006). Slip on the San Andreas fault at Parkfield, California, over two earthquake cycles, and the implications for seismic hazard. *Bulletin of the Seismological Society of America*, *96*(4 B), 283–303. https://doi.org/10.1785/0120050820Nadeau, R. M., & Johnson, L. R. (1998). Seismological studies at Parkfield VI: moment release rates and estimates of source parameters for small repeating earthquakes. *Bulletin of the Seismological Society of America*, *88*(3), 790–814.Nadeau, R. M., & McEvilly, T. V. (1999). Fault slip rates at depth from recurrence intervals of repeating microearthquakes. *Science*, *285*(5428), 718–721. https://doi.org/10.1126/science.285.5428.718Nadeau, R. M., & McEvitty, T. V. (2004). Periodic Pulsing of Characteristic Microearthquakes on the San Andreas Fault. *Science*, *303*(5655), 220–222. https://doi.org/10.1126/science.1090353Noda, H., Lapusta, N., & Kanamori, H. (2013). Comparison of average stress drop measures for ruptures with heterogeneous stress change and implications for earthquake physics. *Geophysical Journal International*, *193*(3), 1691–1712. https://doi.org/10.1093/gji/ggt074Oth, A. (2013). On the characteristics of earthquake stress release variations in Japan. *Earth and Planetary Science Letters*, *377–378*, 132–141. https://doi.org/10.1016/j.epsl.2013.06.037Oth, A.,

Bindi, D., Parolai, S., & di Giacomo, D. (2011). Spectral analysis of K-NET and KiK-net data in Japan, Part II: On attenuation characteristics, source spectra, and site response of borehole and surface stations. *Bulletin of the Seismological Society of America*, *101*(2), 667–687. https://doi.org/10.1785/0120100135Oye, V., Bungum, H., & Roth, M. (2005). Source parameters and scaling relations for mining-related seismicity within the Pyhäsalmi ore mine, Finland. *Bulletin of the Seismological Society of America*, *95*(3), 1011–1026. https://doi.org/10.1785/0120040170Pennington, C. N., Chen, X., Abercrombie, R. E., & Wu, Q. (2021). Cross Validation of Stress Drop Estimates and Interpretations for the 2011 Prague, OK, Earthquake Sequence Using Multiple Methods. *Journal of Geophysical Research: Solid Earth*, *126*(3), 1–24. https://doi.org/10.1029/2020JB020888Ruhl, C. J., Abercrombie, R. E., & Smith, K. D. (2017). Spatiotemporal Variation of Stress Drop During the 2008 Mogul, Nevada, Earthquake Swarm. *Journal of Geophysical Research: Solid Earth*, *122*(10), 8163–8180. https://doi.org/10.1002/2017JB014601Shearer, P. M., Prieto, G. A., & Hauksson, E. (2006a). Comprehensive analysis of earthquake source spectra in southern California. *Journal of Geophysical Research: Solid Earth*. https://doi.org/10.1029/2005JB003979Shearer, P. M., Prieto, G. A., & Hauksson, E. (2006b). Comprehensive analysis of earthquake source spectra in southern California. *Journal of Geophysical Research: Solid Earth*, *111*(6), 1–21. https://doi.org/10.1029/2005JB003979Shearer, P. M., Abercrombie, R. E., Trugman, D. T., & Wang, W. (2019). Comparing EGF Methods for Estimating Corner Frequency and Stress Drop From P Wave Spectra. *Journal of Geophysical Research: Solid Earth*, *124*(4). https://doi.org/10.1029/2018JB016957Sheng, Y., Ellsworth, W. L., Lellouch, A., & Beroza, G. C. (2021). Depth Constraints on Coseismic Velocity Changes From Frequency-Dependent Measurements of Repeating Earthquake Waveforms. *Journal of Geophysical Research: Solid Earth*, *126*(2), 1–12. https://doi.org/10.1029/2020JB020421Sumy, D. F., Neighbors, C. J., Cochran, E. S., & Keranen, K. M. (2017). Low stress drops observed for aftershocks of the 2011 Mw 5.7 Prague, Oklahoma, earthquake. *Journal of Geophysical Research: Solid Earth*, *122*(5), 3813–3834. https://doi.org/10.1002/2016JB013153Thurber, C., Roecker, S., Zhang, H., Baher, S., & Ellsworth, W. (2004). Fine-scale structure of the San Andreas fault zone and location of the SAFOD target earthquakes. *Geophysical Research Letters*, *31*(12), n/a-n/a. https://doi.org/10.1029/2003gl019398Thurber, Clifford, Zhang, H., Waldhauser, F., Hardebeck, J., Michael, A., & Eberhart-Phillips, D. (2006). Three-dimensional compressional wavespeed model, earthquake relocations, and focal mechanisms for the Parkfield, California, region. *Bulletin of the Seismological Society of America*, *96*(4 B), 38–49. https://doi.org/10.1785/0120050825Trugman, D. T. (2020). Stress-drop and source scaling of the 2019 ridgecrest, California, earthquake sequence. *Bulletin of the Seismological Society of America*, *110*(4), 1859–1871. https://doi.org/10.1785/0120200009Trugman, D. T., & Shearer, P. M. (2017). Application of an improved spectral decomposition method to examine earthquake source scaling in Southern California. *Journal of Geophysical Research:*

Solid Earth, *122*(4), 2890–2910. https://doi.org/10.1002/2017JB013971Uchide, T., Shearer, P. M., & Imanishi, K. (2014). Stress drop variations among small earthquakes before the 2011 Tohoku-oki, Japan, earthquake and implications for the main shock. *Journal of Geophysical Research: Solid Earth*, *119*(9), 7164–7174. https://doi.org/10.1002/2014JB010943Waldhauser, F., Ellsworth, W. L., Schaff, D. P., & Cole, A. (2004). Streaks, multiplets, and holes: High-resolution spatio-temporal behavior of Parkfield seismicity. *Geophysical Research Letters*, *31*(18), 2–5. https://doi.org/10.1029/2004GL020649Waldhauser, Felix. (2009). Near-real-time double-difference event location using long-term seismic archives, with application to northern California. *Bulletin of the Seismological Society of America*, *99*(5), 2736–2748. https://doi.org/10.1785/0120080294Waldhauser, Felix, & Schaff, D. P. (2008). Large-scale relocation of two decades of Northern California seismicity using cross-correlation and double-difference methods. *Journal of Geophysical Research: Solid Earth*, *113*(8), 1–15. https://doi.org/10.1029/2007JB005479Wu, Q., Chapman, M. C., Beale, J. N., & Shamsalsadati, S. (2016). Near-source geometrical spreading in the central virginia seismic zone determined from the aftershocks of the 2011 mineral, Virginia, earthquake. *Bulletin of the Seismological Society of America*, *106*(3), 943–955. https://doi.org/10.1785/0120150314Ye, L., Lay, T., & Kanamori, H. (2013). Ground shaking and seismic source spectra for large earthquakes around the megathrust fault offshore of northeastern Honshu, Japan. *Bulletin of the Seismological Society of America*, *103*(2 B), 1221–1241. https://doi.org/10.1785/0120120115Yenier, E., Atkinson, G. M., & Sumy, D. F. (2017). Ground Motions for Induced Earthquakes in Oklahoma. *Bull. Seismol. Soc. Am.*, *107*(1). https://doi.org/10.1785/0120160114Yoshida, K., Saito, T., Urata, Y., Asano, Y., & Hasegawa, A. (2017). Temporal Changes in Stress Drop, Frictional Strength, and Earthquake Size Distribution in the 2011 Yamagata-Fukushima, NE Japan, Earthquake Swarm, Caused by Fluid Migration. *Journal of Geophysical Research: Solid Earth*, *122*(12). https://doi.org/10.1002/2017JB014334Yoshimitsu, N., Ellsworth, W. L., & Beroza, G. C. (2019). Robust Stress Drop Estimates of Potentially Induced Earthquakes in Oklahoma: Evaluation of Empirical Green's Function. *Journal of Geophysical Research: Solid Earth*, *124*(6), 5854–5866. https://doi.org/10.1029/2019JB017483Zeng, X., & Thurber, C. (2019). Three-dimensional shear wave velocity structure revealed with ambient noise tomography in the Parkfield, California region. *Physics of the Earth and Planetary Interiors*, *292*, 67–75. https://doi.org/10.1016/j.pepi.2019.05.007Zhang, H., Liu, Y., Thurber, C., & Roecker, S. (2007). Three-dimensional shear-wave splitting tomography in the Parkfield, California, region. *Geophysical Research Letters*, *34*(24), 1–6. https://doi.org/10.1029/2007GL031951Zoback, M., Hickman, S., & Ellsworth, W. (2011). Scientific drilling into the San Andreas fault zone - An overview of SAFOD's first five years. *Scientific Drilling*, (1), 14–28. https://doi.org/10.2204/iodp.sd.11.02.2011

Strategies	Magnitude dependence	Depth dependence	

Strategies	Magnitude dependence	Depth dependence	
	*0.75-1.75	1.75-2.75	1.
	Slope	R^2	Sl
No temporal correction	1. Single Bin, constant Vs	0.499	0.
	2. Single bin, variable Vs	0.460	0.
	3. Depth bins, constant Vs	0.428	0.
	4. Depth bins, variable Vs	0.404	0.
	5. Spatial Bins, constant Vs	0.384	0.
	6. Spatial Bins, variable Vs	0.354	0.
Temporal correction	1. Single Bin, constant Vs	0.504	0.
	2. Single bin, variable Vs	0.478	0.
	3. Depth bins, constant Vs	0.434	1.
	4. Depth bins, variable Vs	0.409	1.
	5**. Spatial Bins, constant Vs	0.413	0.
	6**. Spatial Bins, variable Vs	0.395	0.
Slope change percentage after temporal correction.	1. Single Bin, constant Vs	1.00%	-
	2. Single bin, variable Vs	3.91%	-
	3. Depth bins, constant Vs	1.40%	-
	4. Depth bins, variable Vs	1.24%	-
	5**. Spatial Bins, constant Vs	7.55%	-
	6**. Spatial Bins, variable Vs	11.58%	-

Table 1. Linear regression results to estimate stress drop dependence on magnitude and depth with different Strategies and temporal correction options. Both magnitude and depth are separated into two ranges with and without apparent scaling (Scaling: Mw0.75-1.75, Non-scaling: Mw1.75-2.75). An example to calculate slope change percentage: for Strategy 4, 11.58%=(0.395-0.354)/0.354*100%.

*The magnitude scaling range is determined in Figure S7 by calculating the slope between a certain magnitude and Mw2.75. When Mw>1.75, such slopes become centered at 0 for most of the Strategies, meaning the flat part starts from around Mw1.75.

**Note that for 5 and 6, the ECSs for each spatial bin is corrected using the ECSs from depth-binning only in Strategy 3 from corresponding time periods.

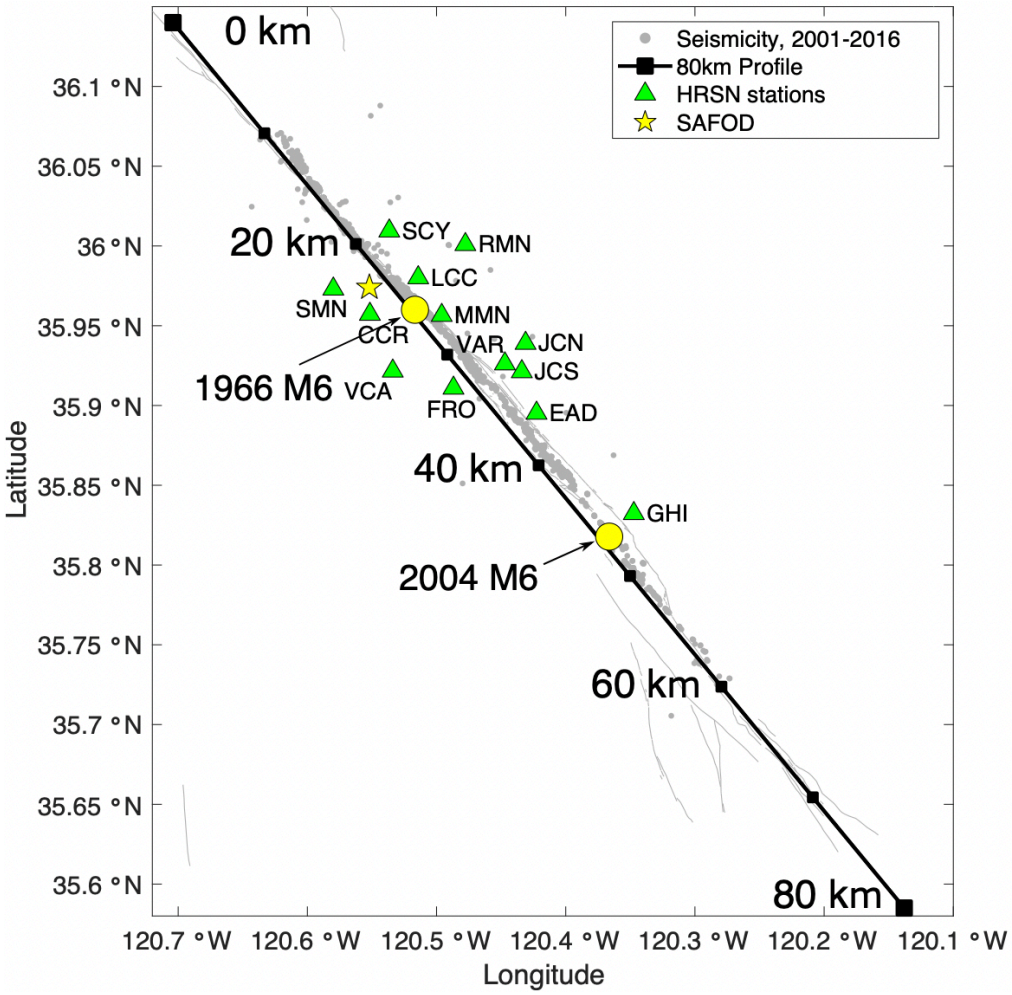

Figure 1. Seismicity map of research area. Fault lines (thin grey lines) are obtained from USGS, and event locations (grey circles) follow the double-difference catalog by Waldhauser and Schaff (2008). The HRSN stations (green triangles) and the SAFOD (San Andreas Fault Observatory at Depth) locations are obtained from NSCN (Northern California Seismic Network). The two yellow circles indicate the locations of the 1966 and 2004 M6 earthquakes. The black solid line indicates the study area from 0 to 80 km along strike.

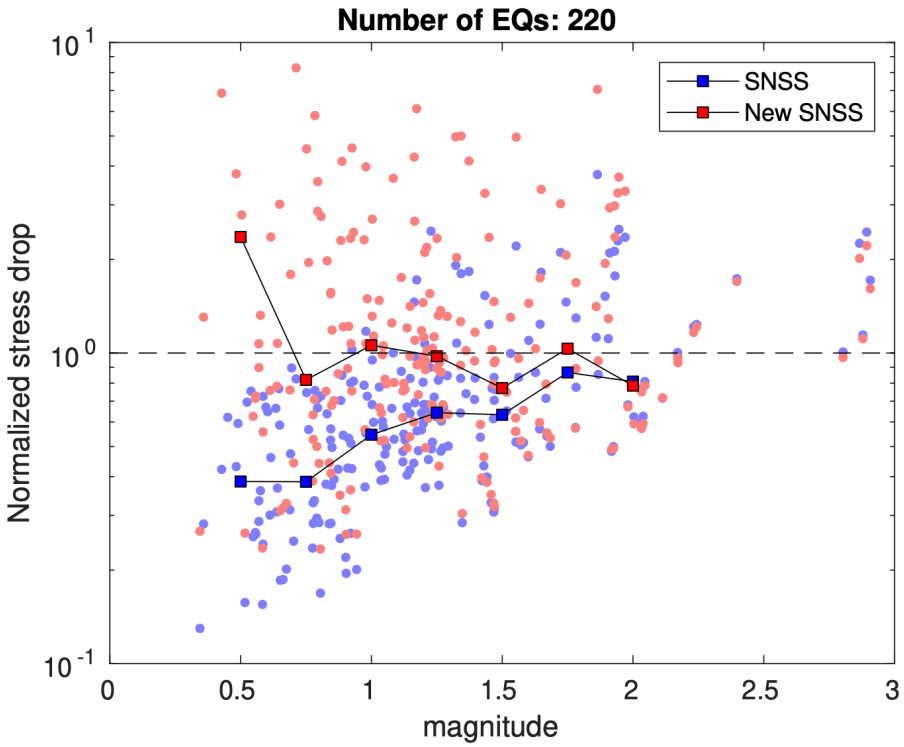

Figure 2. Comparison between the SNSS method (blue) and the new hybrid SNSS method (red) in terms of magnitude dependence, using 220 earthquakes selected from depth between 4-5km depth and 30-40km from NW end of SAF profile (see Figure 1 for the distance range). Y-axis represents the 'normalized stress drop', which is calculated by dividing the individual event stress drops by the median of stress drop of M>1.5 events. The squares show the median of normalized stress drop in magnitude bins [0.5:0.25:3] with the bin size of 0.5 from the corresponding methods.

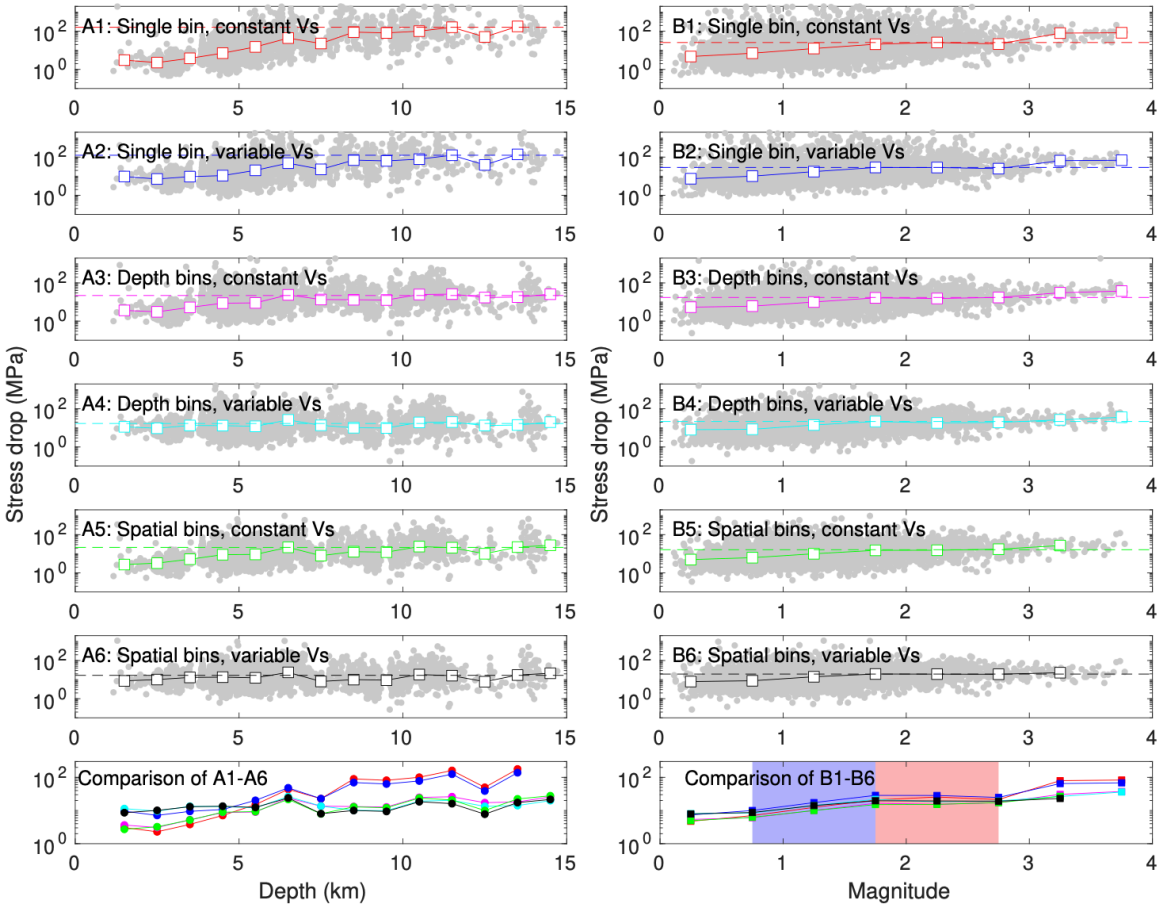

Figure 3. Complete comparison among different strategies for stress drop depth dependence (A1-A6) and magnitude dependence (B1-B6). The sixth strategy (A6 and B6) is the preferred strategy. The gray dots represent the stress drop measurements, and the squares are the median values calculated in 1km depth bin for depth dependence (A1-A6) and M0.5 bin magnitude dependence (B1-B6). In the bottom right panel, the light blue box indicates magnitude ranges with magnitude dependence (M0.75-1.75), while the light red box indicates magnitude ranges with no magnitude dependence (M1.75-2.75).

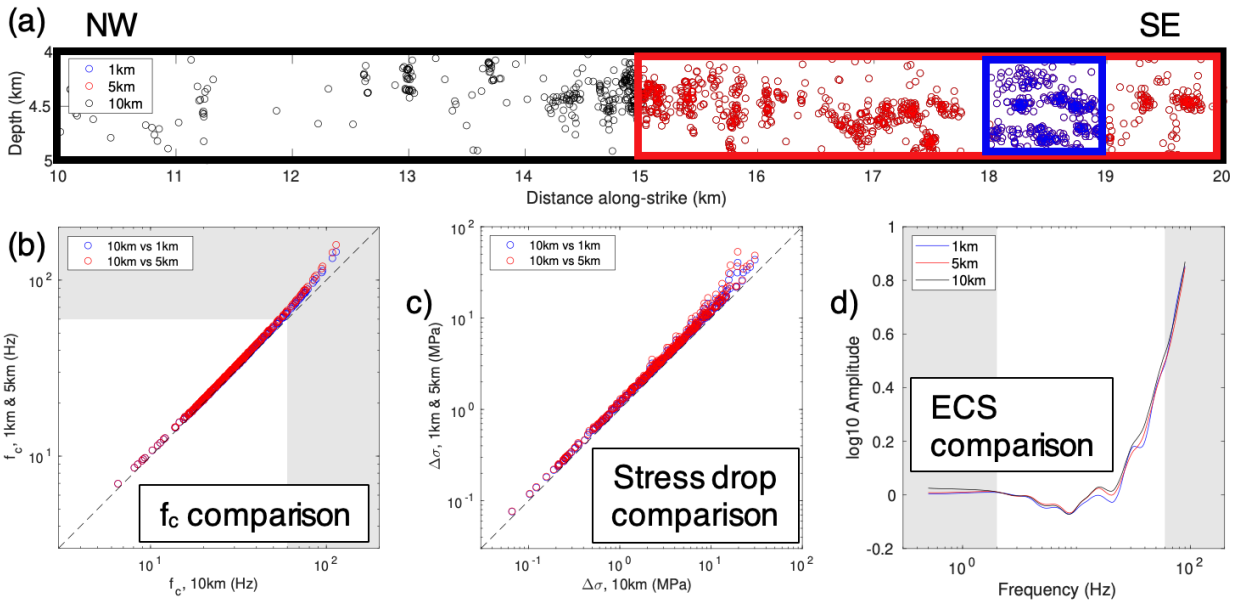

Figure 4. Comparison of the influence of bin size. (a) Bin size selection, 1km (blue), 5km (red) and 10km (black) along strike and 1km depth range. (b) Corner frequency comparison between 10km bin and 1km (blue) and 5km (red) bin. (c) Stress drop comparison between 10km bin and 1km (blue) and 5km (red) bin. (d) ECSs solved from different bin sizes. Shaded areas in (b) and (d) represent frequency band outside the fitting range (higher than 60Hz, or lower than 2Hz). Black dashed lines in (b) and (c) indicate identical values. The comparison indicate 10 km along strike box can sufficiently account for attenuation at 1 km, and the 10km-by-1km area is selected for data analysis because of its high event density. The 10km test area is highlighted in Figure 6(a) as a black box.

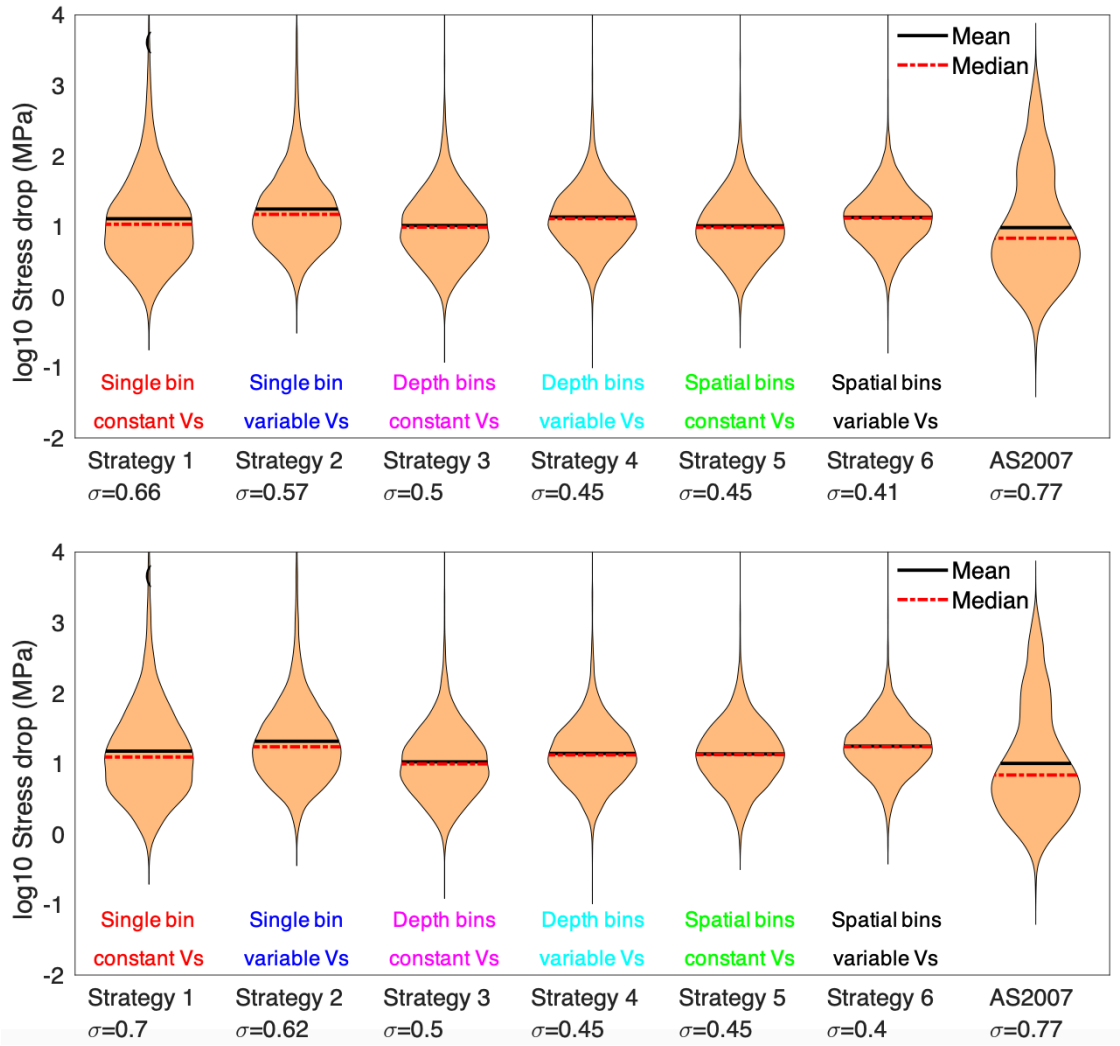

Figure 5. Histogram of stress drop estimates of AS2007 and before (a), after (b) temporal correction per strategy. The standard deviation of log10 stress drops in listed beneath each histogram. The black and red dashed bars represent log10 of mean and median stress drops for each case.

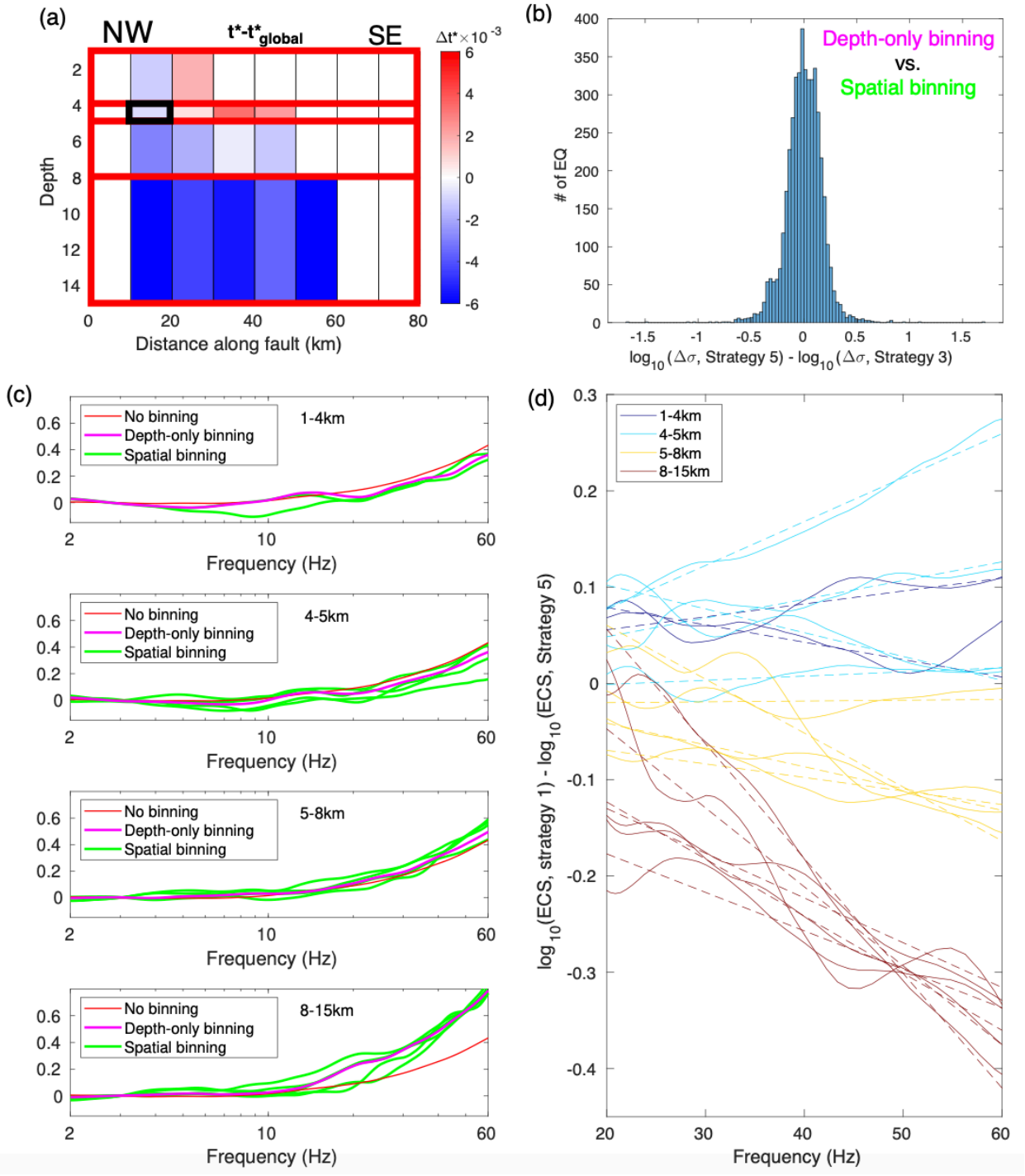
(a)
NW
t*-t*global
SE
Δt*×10-3
Depth
Distance along fault (km)
(b)
Depth-only binning
vs.
Spatial binning
# of EQ
log10(Δσ, Strategy 5) - log10(Δσ, Strategy 3)
(c)
No binning
Depth-only binning
Spatial binning
1-4km
4-5km
5-8km
8-15km
Frequency (Hz)
(d)
1-4km
4-5km
5-8km
8-15km
log10(ECS, strategy 1) - log10(ECS, Strategy 5)
Frequency (Hz)

Figure 6. Comparison of spatial variation of attenuation. (a) t* variability among both the horizontal and vertical bins with values derived from the linear fitting of the difference between ECSs in all the bins from Strategy 5 and the ECS from Strategy 1. Note the layered distribution along depth, indicating depth is the major factor in affecting attenuation correction. Thick black box indicates the 10km by 1 km spatial bin used in the test shown in Figure 4. (b) Histogram of log10 stress drop difference of individual earthquakes between Strategy 3 and 5. (c) ECSs from different Strategies in different horizontal bins for different depth ranges (Red: Strategy 1 with no spatial binning, which is identical in different depths; Magenta: Strategy 3 with depth-only binning; Green: Strategy 5 with spatial binning). (d) Strategy 5 ECSs subtracted by Strategy 1 ECS, different horizontal bins from the same depth range share the same color. Dashed lines are linear fit to the solid curves between 20Hz and 60Hz, and their slopes are used to evaluate t* variation over space in (a).

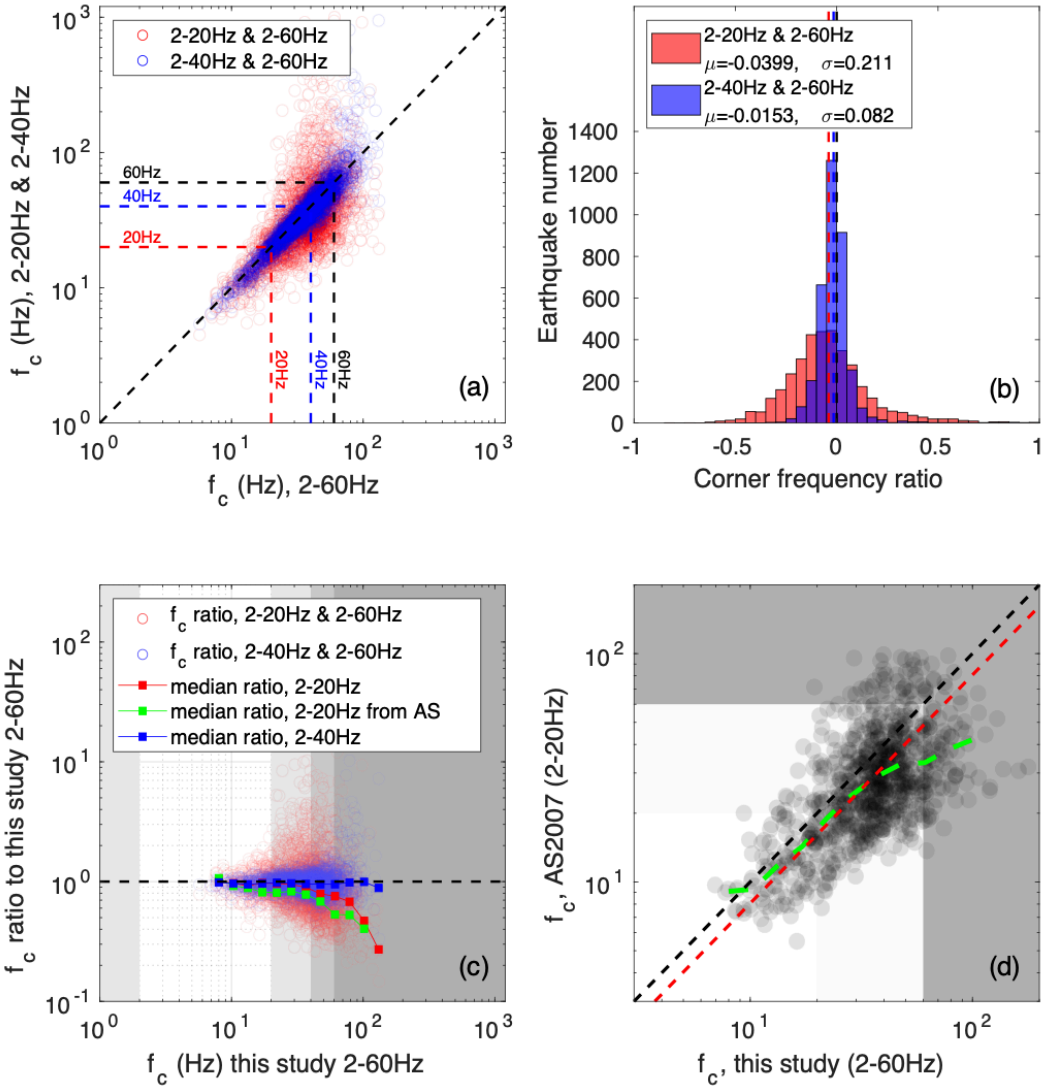

Figure 7. Comparison of the influence of bandwidth limit by using different frequency ranges (2-20Hz, 2-40Hz and 2-60Hz) for corner frequency estimation. (a) Comparison of individual event corner frequency inverted with different frequency ranges indicated by different colors. (b) Histogram of log10 corner frequency ratio between 2-20Hz and 2-60 Hz (red), and between 2-40Hz and 2-60Hz (blue). Red and blue vertical dashed lines show the mean values of both cases, and the black vertical dashed line is 0. (c) Corner frequency ratio between various methods and 2-60 Hz versus corner frequencies from 2-60 Hz. Red dots are 2-20 Hz and blue dots are 2-40 Hz. Median values (red and blue squares) are calculated from events with 2-60 Hz corner frequency between 2 and 100

Hz, a minimum of 5 earthquakes is required to calculate median values. Green squares are the median ratio using AS2007 results (2-20 Hz from surface network). Black horizontal dashed line indicates ratio of 1. Areas with different darkness represent corner frequencies outside of 2-20Hz, 2-40Hz and 2-60Hz. (d) Comparison of individual earthquake corner frequencies between this study and AS2007 (transparent black circles). Black dashed line represents where two studies are consistent and red represents where corner frequencies in this study (2-60 Hz) are 1.5 times of those in AS2007. The white area indicates the frequency limit in AS2007 (20Hz), the light gray area between the frequency limits of AS2007 (20Hz) and this study (60Hz), and the dark gray area higher than the frequency limit in this study (60Hz). The green dashed curve is the median of corner frequencies of AS2007 relative to those in this study (similar to the green line in figure c).

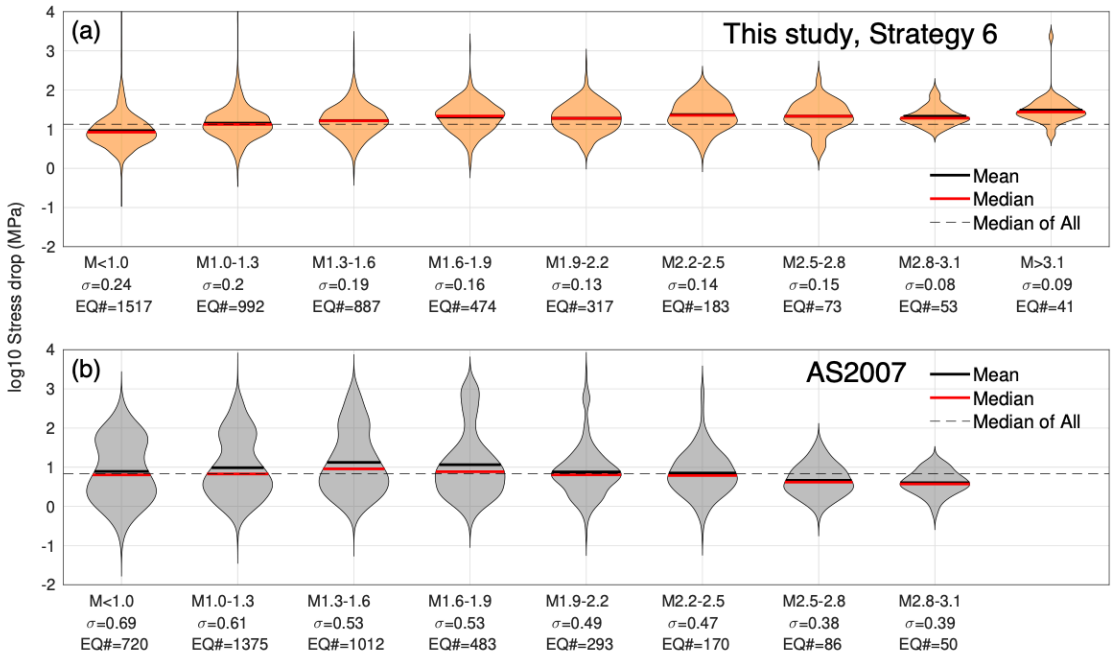

Figure 8. Violin plot of stress drops by magnitude for this study using Strategy 6 after temporal correction (a, yellow) and AS2007 (b, grey). Black and red bars represent mean and median values in each magnitude range. The horizontal dashed lines are showing the median values for all the stress drops in both studies, respectively.

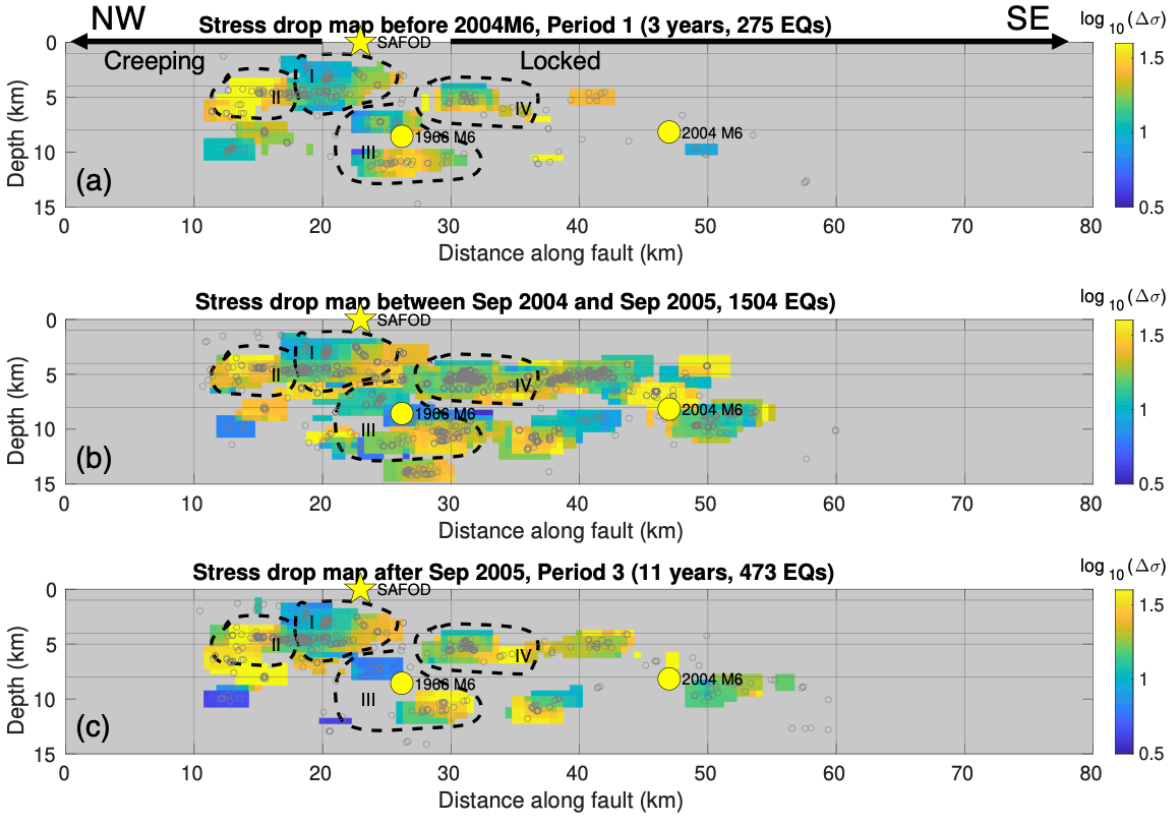

Figure 9. Spatial distribution of stress drop in the 3 time periods (a-c) with only Mw>1.1 earthquakes, coded by the log10 stress drop values in every 4km-by-2km block for grids at increment of 0.5km both horizontally and vertically. The yellow star is the location of SAFOD, and yellow circles are the locations of the 1996 M6 and 2004 M6 earthquakes. The gray open circles are the seismicity included in this study. Dashed curves outline four regions for detailed discussion: I. SAFOD area, II. Creeping Zone, III. 1966 M6 area, IV. Locked zone.

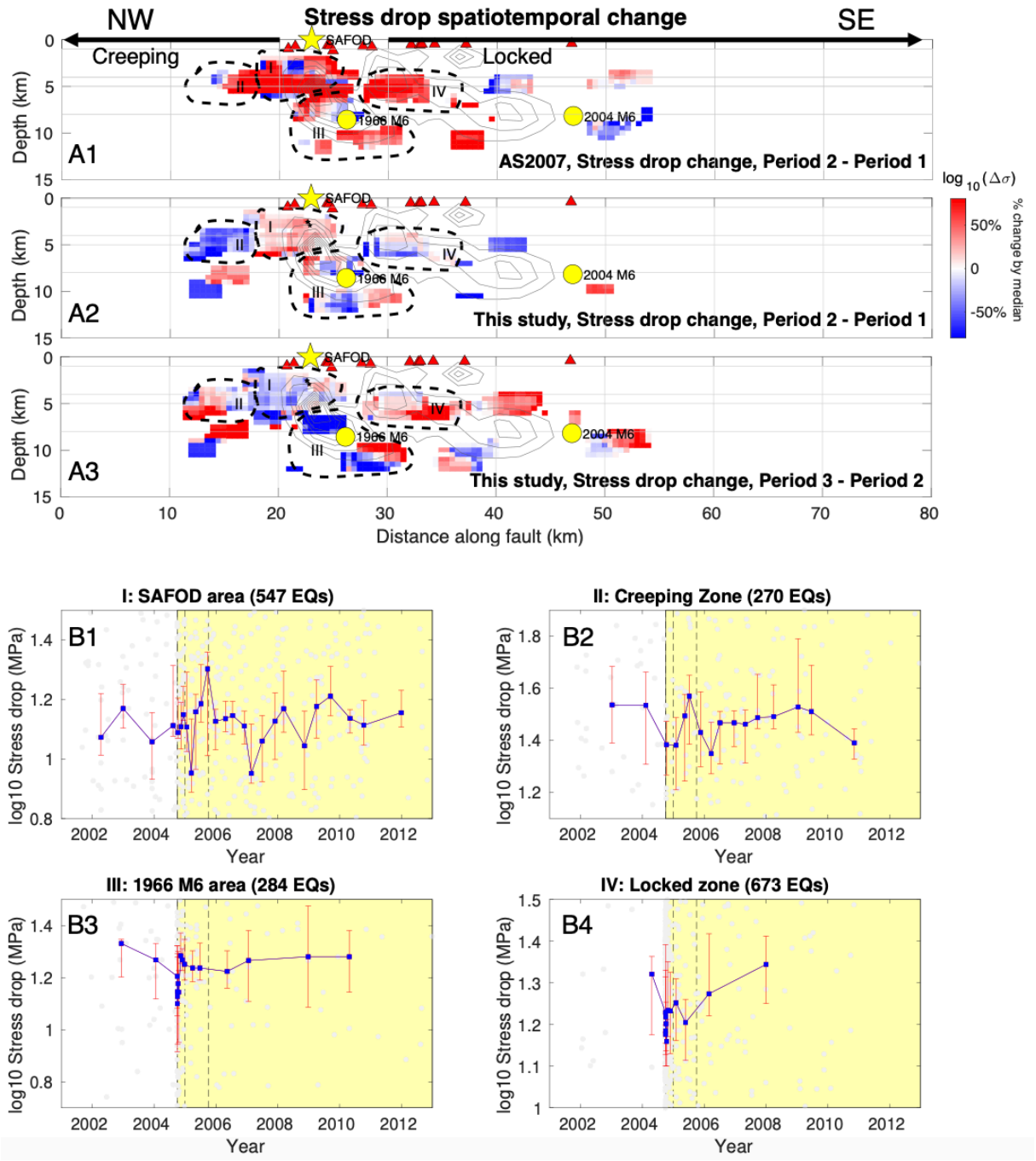

Figure 10. Stress drop change among the 3 time periods indicated in Figure 9 using only Mw>1.1 earthquakes. (A1) Difference between pre-Sep 2004 and

Sep 2004-Sep 2005 using AS2007 results for comparison with A2. (A2) Difference between pre-Sep 2004 and Sep-2004 and Sep-2005 from this study. (A3) Difference between Sep 2004-Sep 2005 and post-Sep 2005 from this study. Color represents the percentage of log10 stress drop difference of the over stress drop standard deviation to describe stress drop variations over time and space. (B1-B4) Stress drop temporal change in the four regions outlined by dashed curves: I. SAFOD area, II. Creeping Zone, III. 1966 M6 area, IV. Locked zone, where the blue squares are the median stress drop over time calculated from every certain earthquakes (vary by area), and the red error bars describe the range of median stress drops calculated by 30 times of bootstrapping resampling, each resample contains 70% of the earthquakes for each blue square. Two vertical dashed lines mark the 3-month and 1-year after 2004 M6 earthquake.

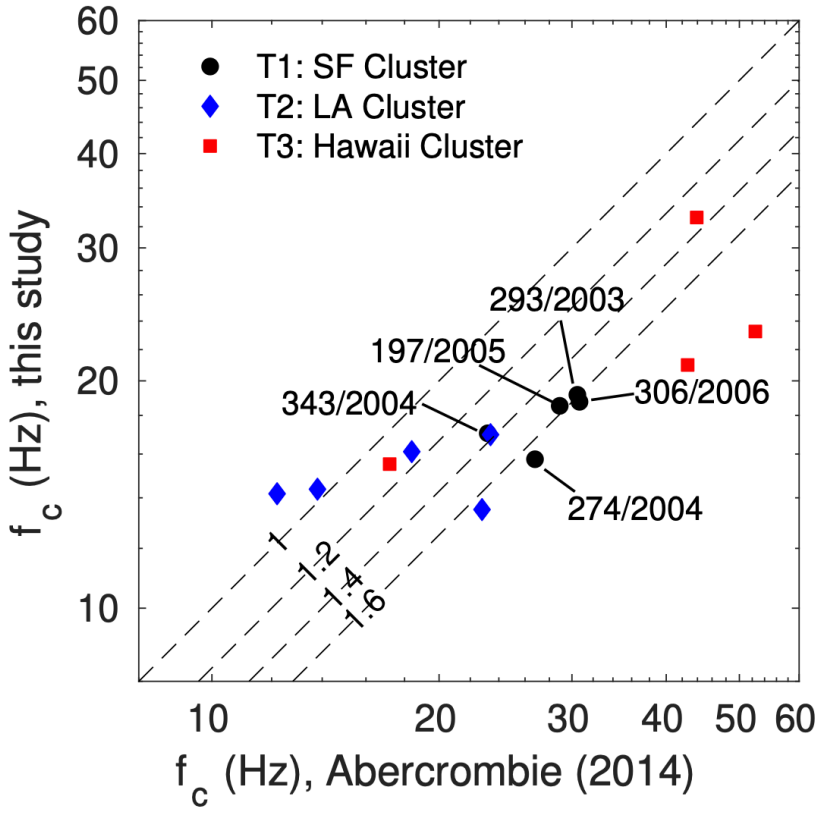

Figure 11. Comparison of individual corner frequencies in this study and those in Abercrombie (2014). Different colors and markers shown in the legend represent different SAFOD targeted clusters. Different dashed lines indicate the factor (numbers on the lines) relative to the fc of this study. The Julian days and years of the events in cluster T1 are marked in the figure; for reference, the 2004 Parkfield M6 occurred on 272/2004.

Journal of Geophysical Research

Supporting Information for

Spatiotemporal variability of earthquake source parameters at Parkfield, California, and their relationship with the 2004 M6 earthquake

Jiewen Zhang[1], Xiaowei Chen[1], Rachel Abercrombie[2]

[1]University of Oklahoma, Norman Oklahoma

[2]Boston University, Boston Massachusetts

Contents of this file

Figures S1 to S11

Additional Supporting Information (uploaded as a separate file)

Data file containing information of 4537 earthquakes: qinfo.dat

Data description in the file:

The file lists date & time, location, event ID and stress drop & corner frequency information of all 4537 earthquakes. First row of the file shows the variable name of each column. Except for Mw, stress drop and corner frequency (f_c), all other information is in the Northern California double-difference catalog (WNC catalog, Waldhauser, 2009; Waldhauser & Schaff, 2008), downloaded from Northern California Earthquake Data Center (NCEDC); Mw represents moment magnitude obtained in this study after magnitude calibration from NCEDC catalog, and stress drops & corner frequencies are from Strategy 6 with temporal corrections (see the main texts).

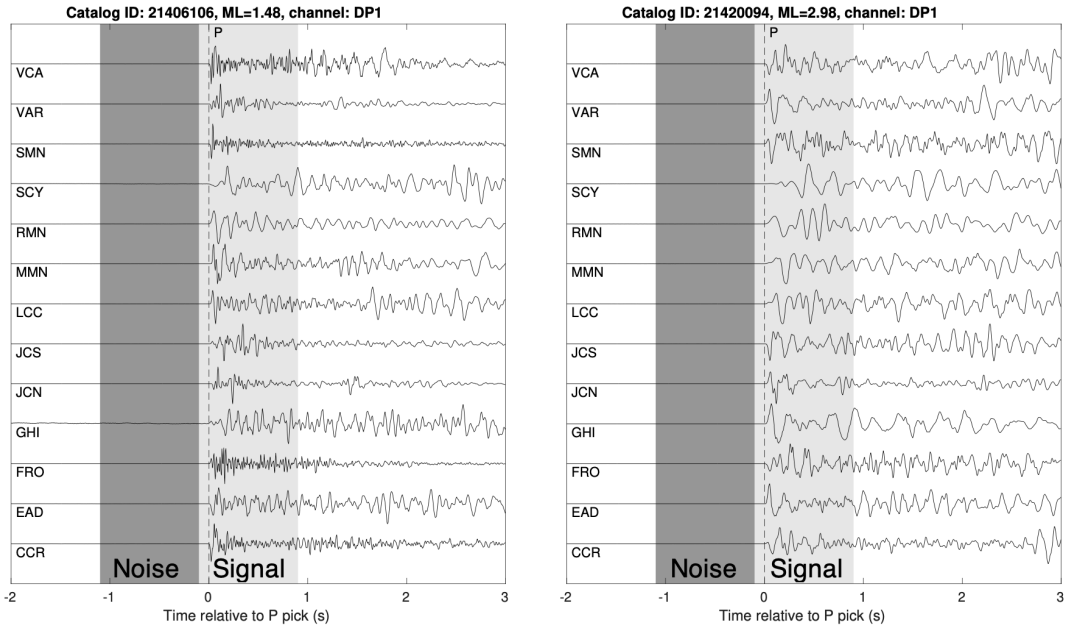

Figure S1. Example waveforms of two earthquakes recorded at HRSN stations with different magnitudes used in the stress drop estimation. Waveforms are aligned by P arrival picks at the stations. Dark and light gray areas represent the P noise (1s) and signal (1s) windows for spectrum computation. The signal window starts from -0.1s of the P arrivals and ends at 0.9s after the P arrivals.

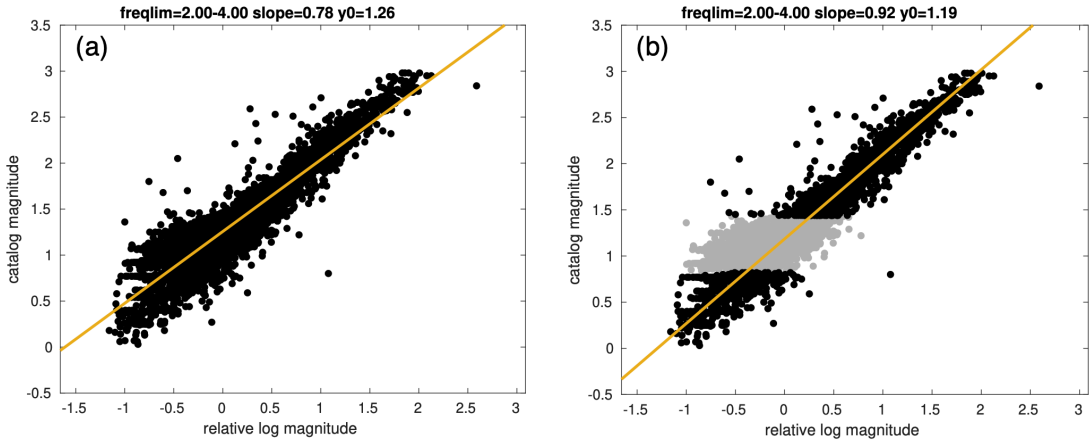

Figure S2. Magnitude calibration, individual earthquakes are shown as black dots. (a) The abnormal amplitudes at around M1 result in biased linear fitting (slope=0.78). (b) After removing M0.83-M1.40 earthquakes (gray dots) in the calibration, we obtain slope=0.92 and the linear fitting is more reasonable. Note that the earthquakes removed from calibration are still included in the spectral

analysis.

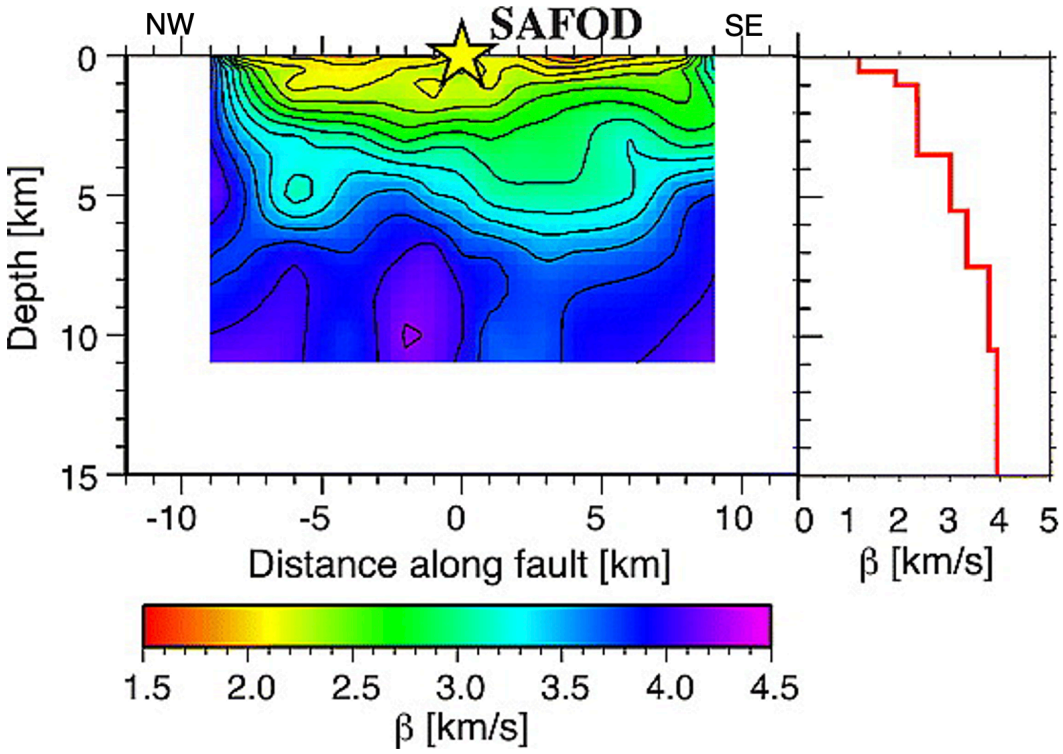

Figure S3. Velocity model for depth-varying rupture velocity (Allmann and Shearer, 2007, Figure 5). Within the scale of 10km, the velocity variation along strike similar to that in the scale of 1km over depth, and vertically the velocity model shows significant velocity contrast. The velocity model validates our spatial bin size selection as in Figure S5.

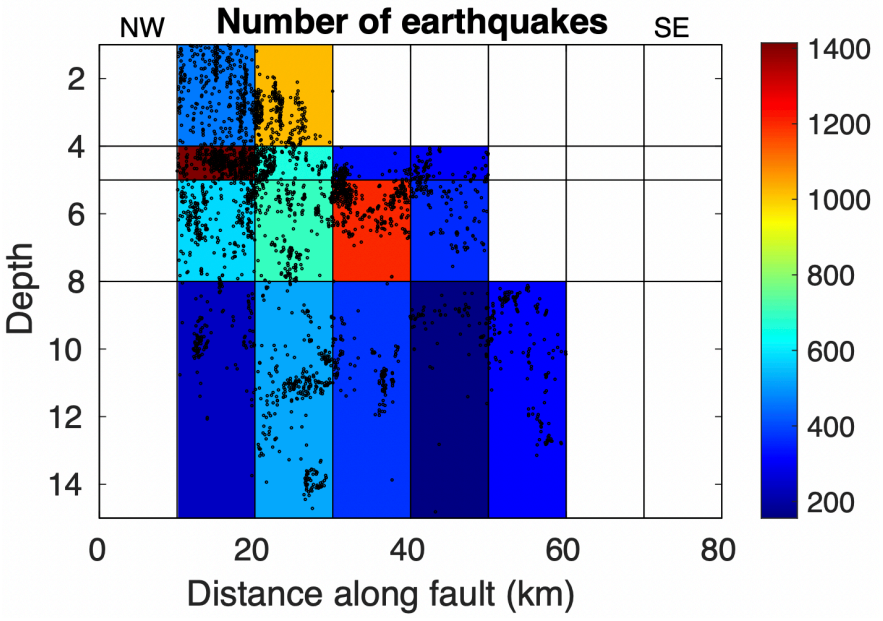

Figure S4. Spatial bins setup, totally 32 bins, the 15 bins with earthquakes more than 200 are included in the final analysis to ensure stability of the SNSS method. Color indicates the number of earthquakes in each bin.

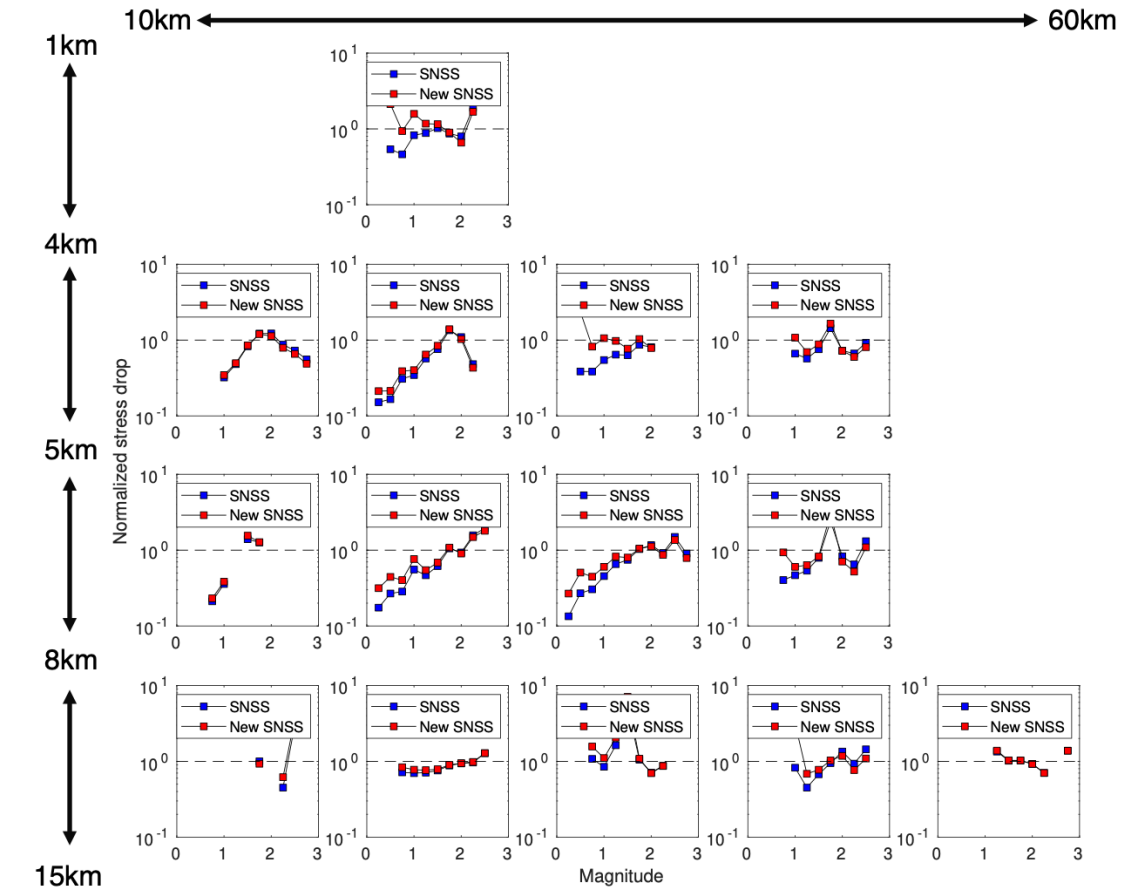
10km
60km
1km
4km
5km
8km
15km
SNSS
New SNSS
Normalized stress drop
Magnitude

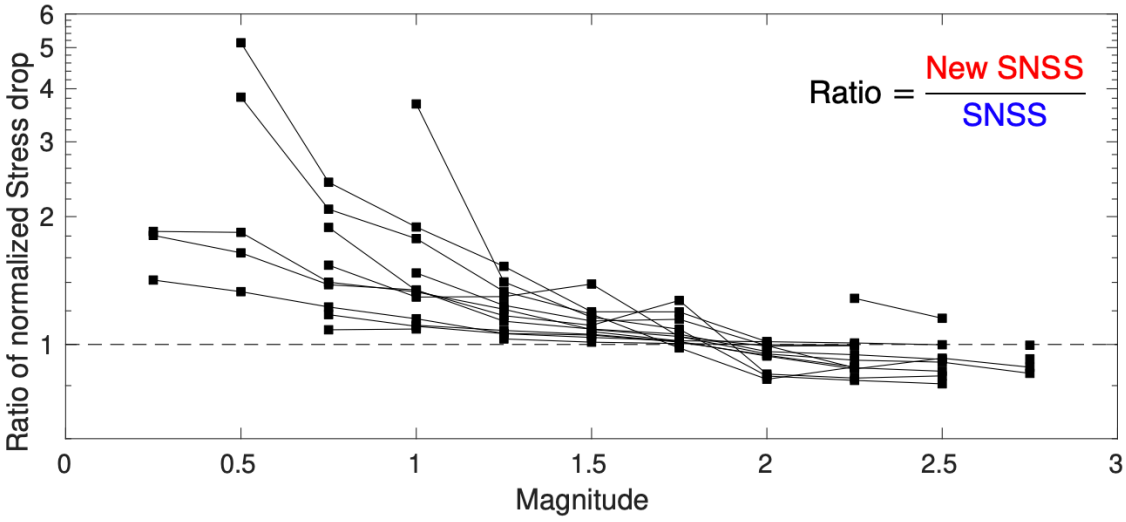
Ratio of normalized Stress drop
Magnitude
Ratio = New SNSS / SNSS

Figure S5. Comparison of the new hybrid SNSS and the original SNSS methods. (a) Per spatial bin, normalized stress drop (by median of stress drop for M>1.5) VS magnitude between the new hybrid SNSS method (blue) and the original SNSS method in Chen & Abercrombie (2020) (red). Squares are the median values calculated for magnitude bins at 0.25 interval with 0.5 bin size. (b) Compiled results of hybrid SNSS results (red) divided by SNSS (blue) in different spatial bins in the top panel.

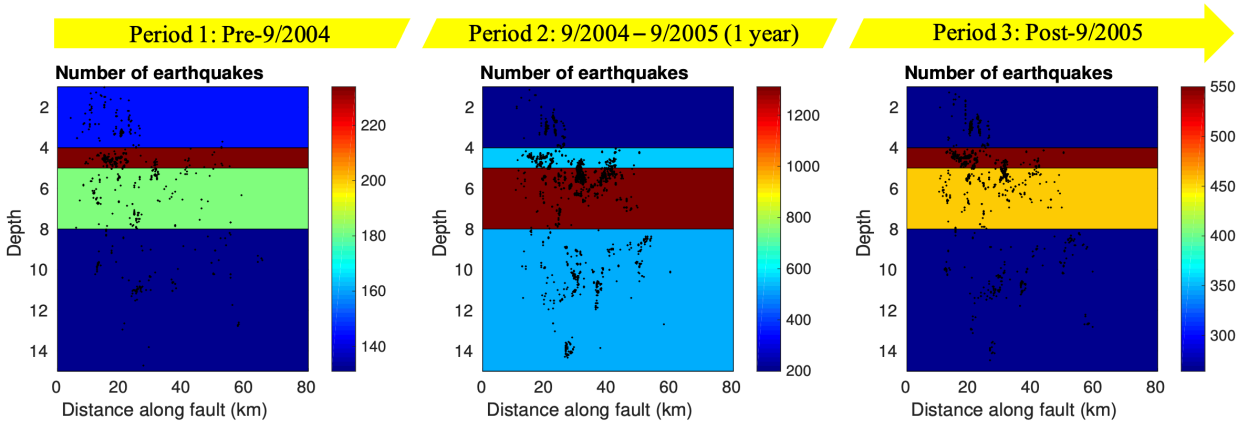

Figure S6. Three time periods and the earthquake distribution in the layered bins accounting for temporal attenuation variations (Period 1: pre-2004 M6, Period 2: one-year period after 2004 M6, Period 3: After the one-year period). Only depth bins are applied with colors showing the number of earthquakes with at least 5 station records in the bins.

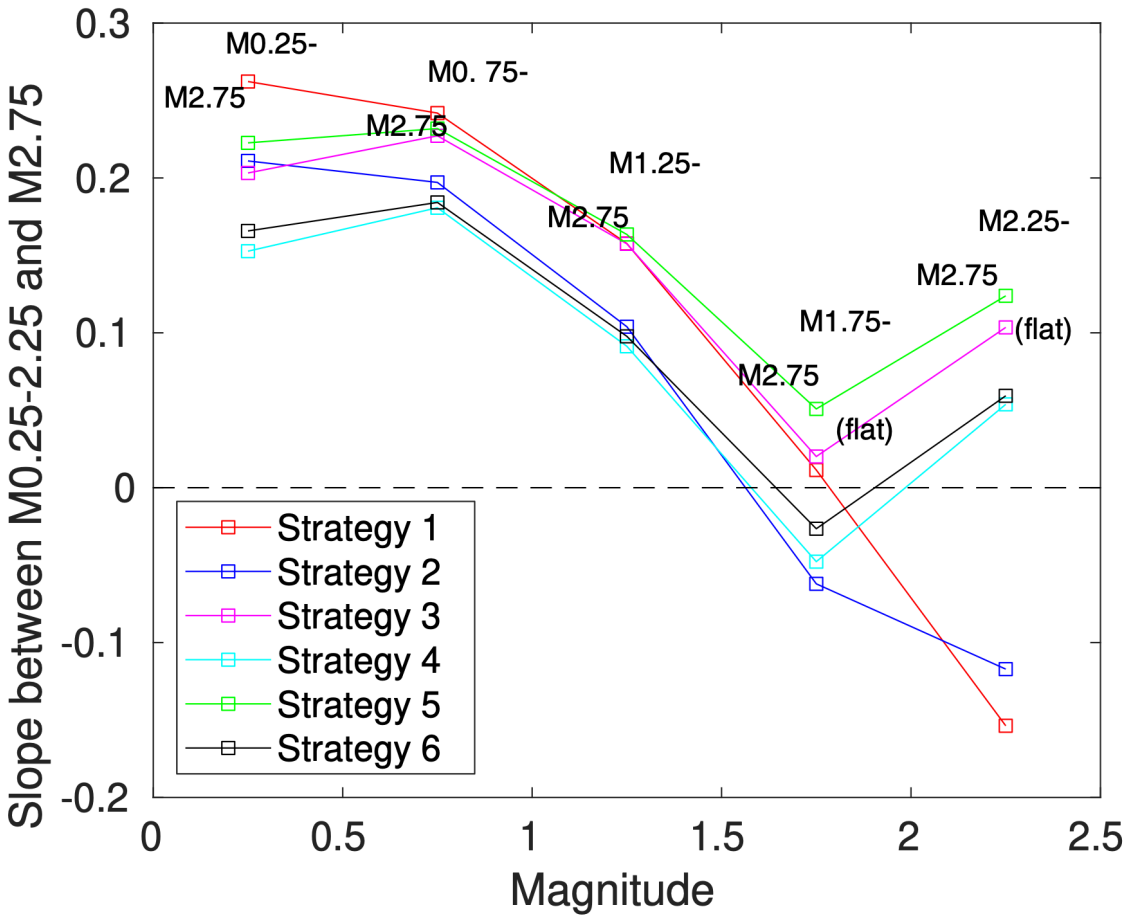

Figure S7. Magnitude scaling factor between M0.25/0.75/1.25/1.75/2.25 and M2.75 after temporal attenuation correction for different strategies. This figure is used to examine which magnitude range has more significant scaling. Different colors represent Strategies from 1 to 6. A slope close to 0 means there is no scaling between a certain magnitude and M2.75.

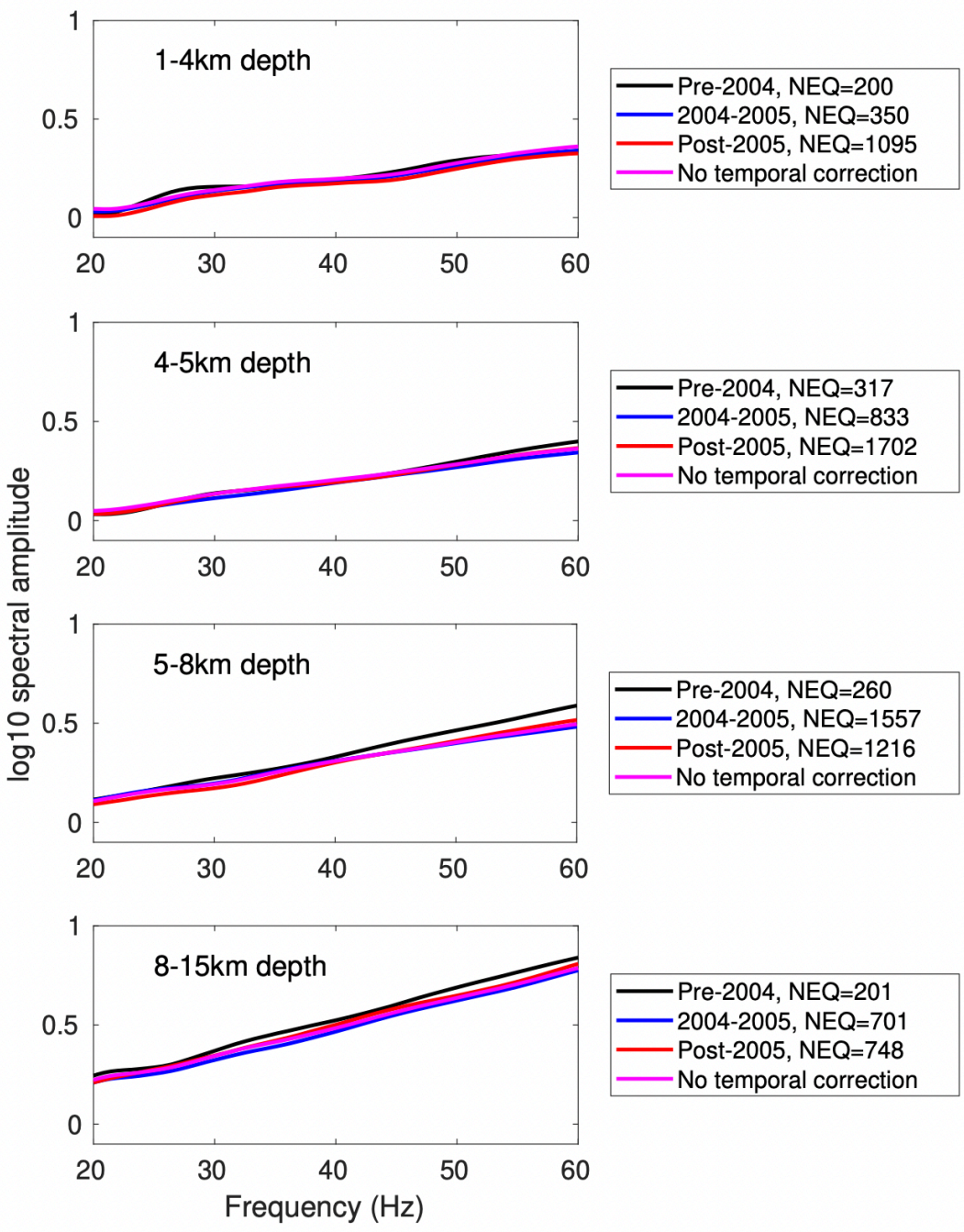

Figure S8. ECS temporal change in different depth ranges (Black: before Sep. 2004, Blue: Sep. 2004 - Sep. 2005, Red: after Sep. 2005) when only considering

depth binning. This is to show the potential attenuation change over time at different depths.

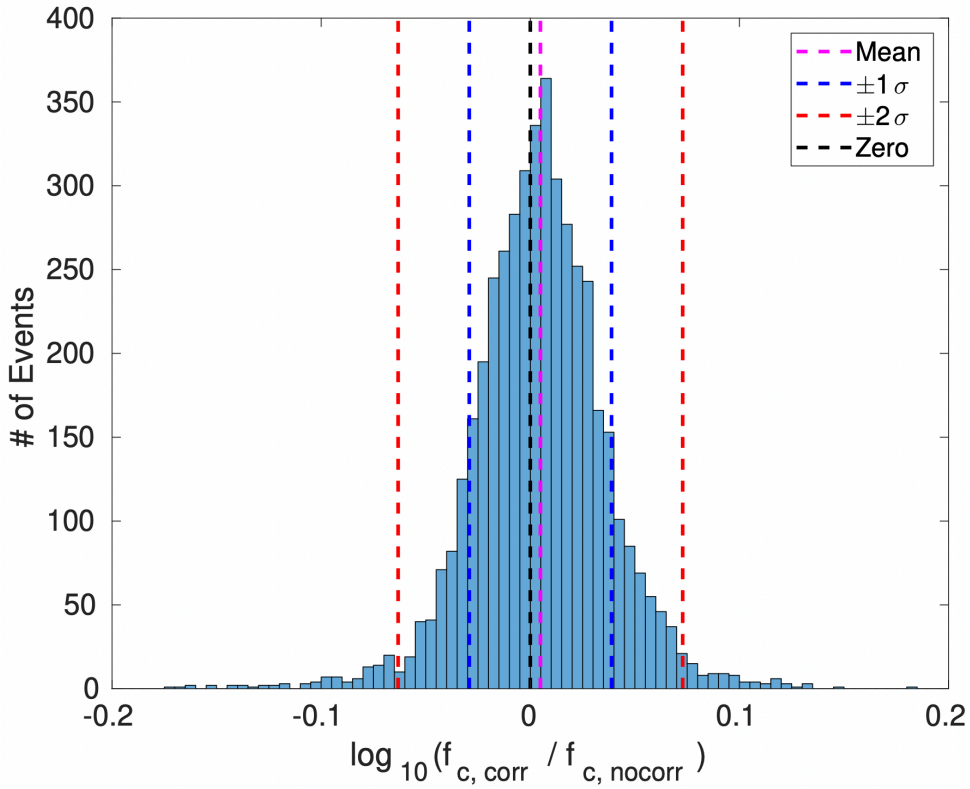

Figure S9. Difference of corner frequencies of individual events between temporal correction and non-temporal correction. The difference is measured by the log10 of ratio between the individual corner frequencies for individual events in the two cases. The average of difference m is 0.0048 (1.011 times of difference) shown as magenta dashed line in comparison to the black dashed line (indicating no difference), and the standard deviation s is 0.034 with blue dashed lines showing $m \pm s$ (76.3% of total events) and red dashed lines showing $m \pm 2s$ (95.2% of total events).

(a)

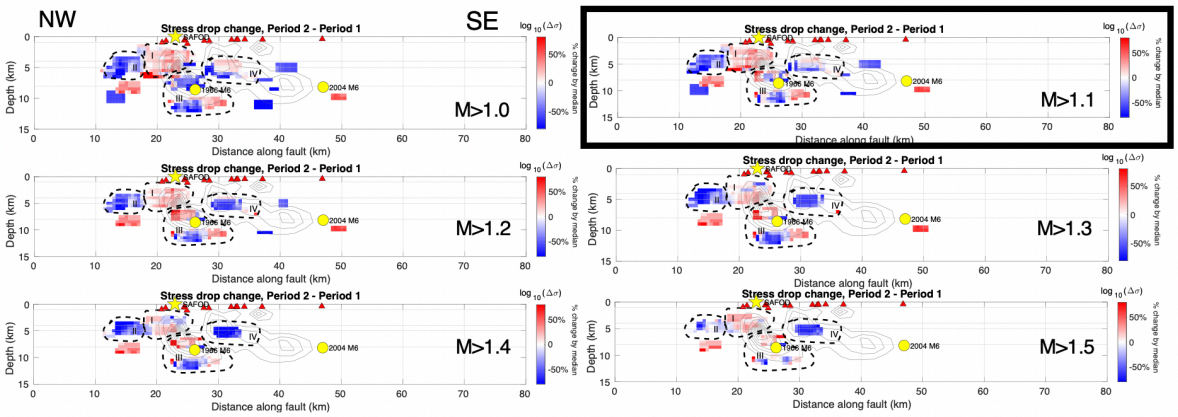

(b)

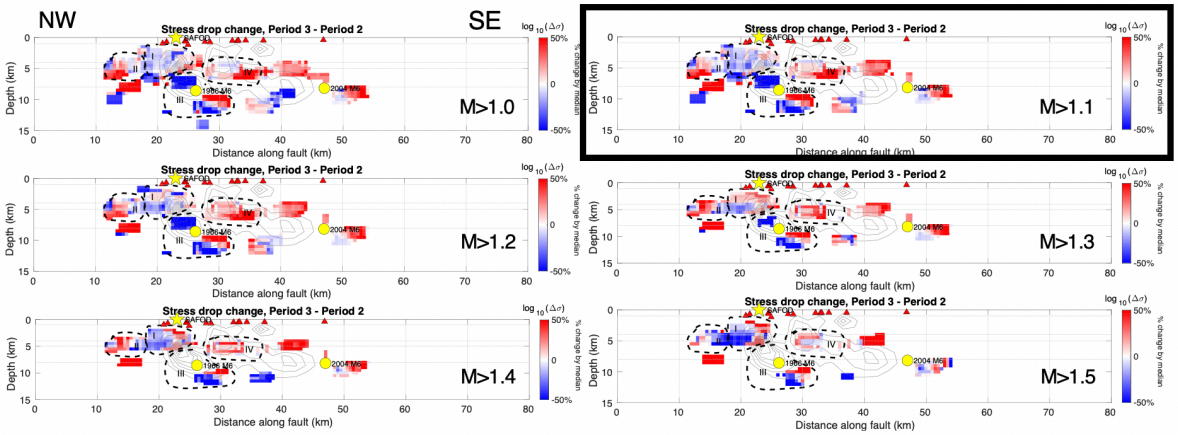

(Continued in the next page)

(Continued)

(c)

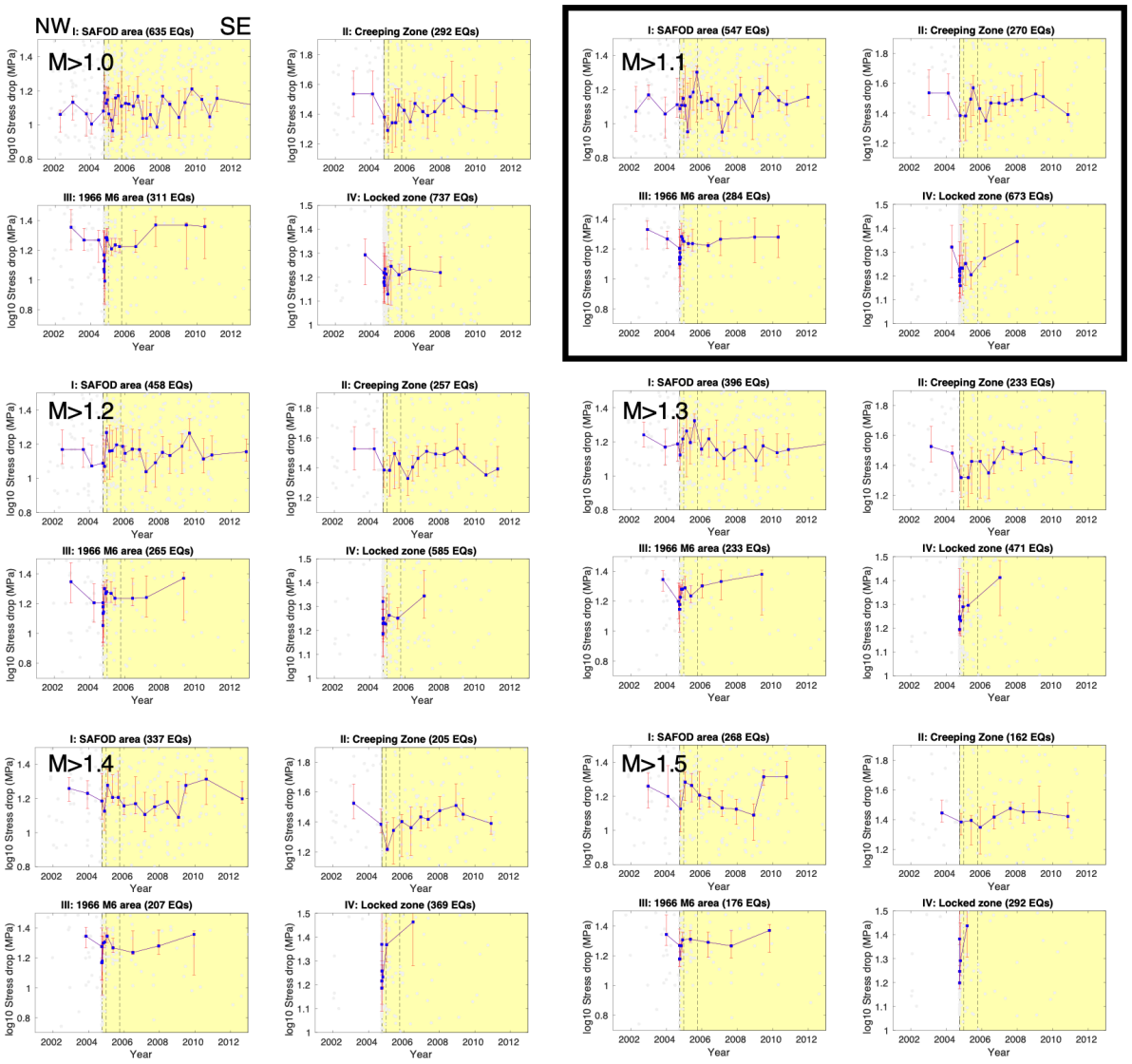

Figure S10. A demonstration of how magnitude threshold affects stress drop spatiotemporal changes. (a) difference between pre-Sep 2004 and Sep 2004-Sep 2005, with different magnitude thresholds, (b) Difference between Sep 2004-Sep 2005 and post-Sep 2005, and (c) the detailed temporal change within the 1966 M6 slip patch marked with black dashed lines for different magnitude thresholds. All the items in this figure share the same meanings as those in Figure 10. Black squares point out the threshold used for final results. In each panel above, only the first subplot has NW and SE marks indicating the direction of the section

on the SAF, and all the other subplots follow the same direction.

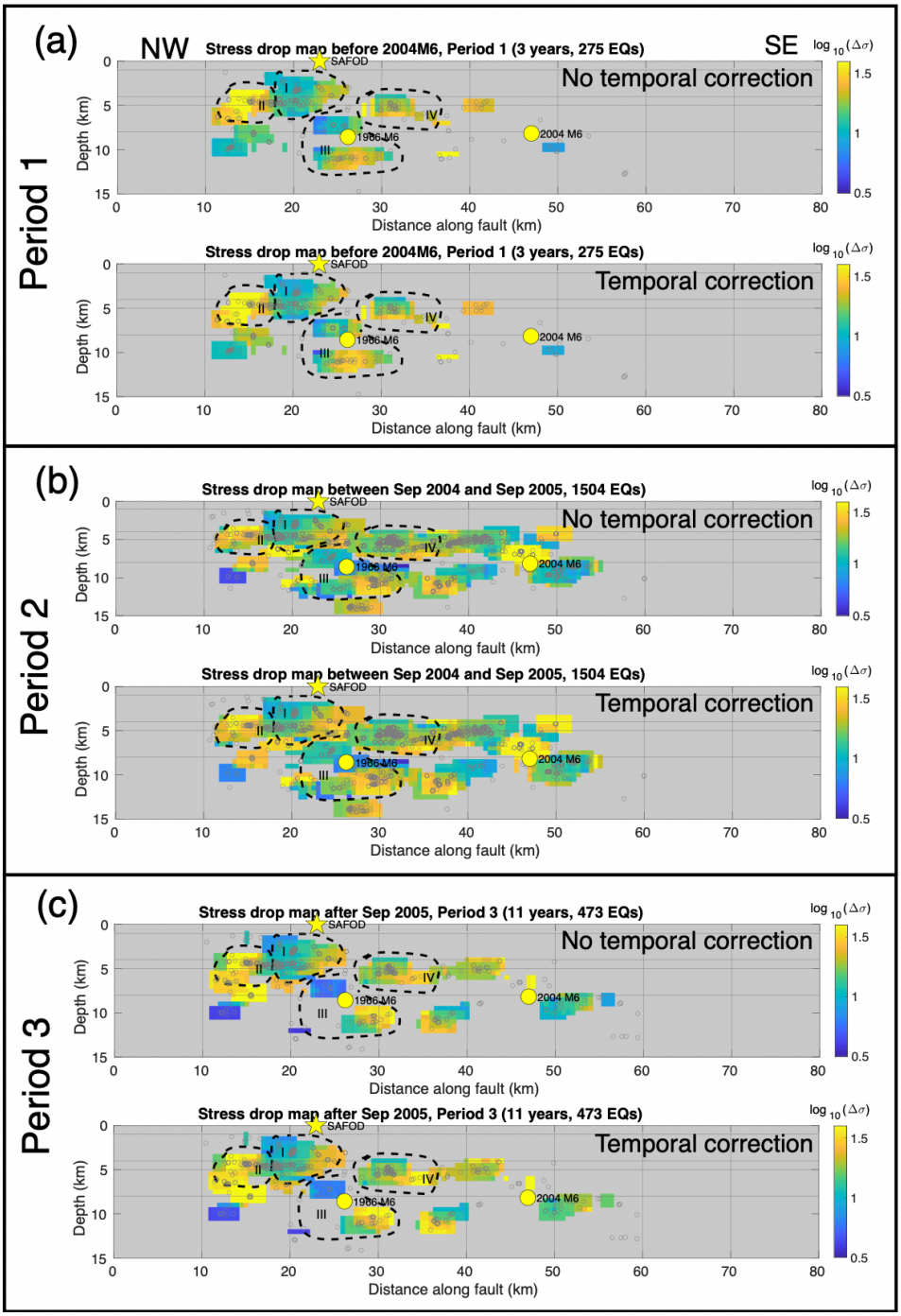

Figure S11. Comparison of spatial patterns of stress drop before and after temporal attenuation correction. The spatial distributions are remarkably similar, indicating the influence of temporal attenuation is minimal. Only Mw>1.1 earthquakes are included. (a-c) represent the comparison in 3 different time periods described in the texts.